

**Incorporating the SSM/I-derived Precipitable  
Water and Rainfall Rate into a Numerical Model:  
A Case Study for ERICA IOP-4 Cyclone**

Q. Xiao and X. Zou

*Dept. of Meteorology, Florida State University, Tallahassee, FL 32306-4520*

Y.-H. Kuo

*MPG/MMM/NCAR, P. O. Box 3000, Boulder, CO 80307-3000*

Submitted to Mon. Wea. Rev. on March 20, 1998

**DISTRIBUTION STATEMENT A**  
Approved for Public Release  
Distribution Unlimited

DTIC QUALITY INSPECTED 4

19991122 064

## ABSTRACT

In this paper, a variational data assimilation approach is used to assimilate the rain rate (RR) data together with precipitable water (PW) measurements from Experiment on Rapidly Intensifying Cyclones over the Atlantic (ERICA) (4-5 January 1989; IOP-4 cyclone). The PW and RR, which are assimilated into the MM5 model, are computed from the Special Sensor Microwave/Imager (SSM/I) raw data—brightness temperatures, via a statistical regression method. The SSM/I-derived RR and PW at 0000 UTC and/or 0930 UTC are assimilated into the MM5. The data at 2200 UTC are used for verification of the prediction results. Numerical experiments are performed using the Penn State/NCAR mesoscale model version 5 (MM5). Two horizontal resolutions of 50 *km* and 25 *km* are used in our studies. Comparisons are made between the experiments with and without SSM/I-measured PW and RR observations. Results from these experiments showed that:

1) The MM5 simulated a well-behaved but slightly less intense, position-shifted cyclogenesis episode based on the NCEP analysis enhanced with only radiosonde and surface observations through a Cressman-type of objective analysis.

2) The satellite-derived PW and RR observations were assimilated successfully into the MM5 model by a variational method. The cost function which measures the distance between the model predicted and the observed PW and RR decreased by about one order of magnitude.

3) Assimilation of PW and RR significantly improved the cyclone prediction, reflected mostly in the cyclone's track, the associated frontal structure and the associated precipitation along the front. The model's spin-up problem during the simulation was greatly reduced after assimilating the PW and RR information into the model initial conditions.

4) Sensitivity experiments of RR assimilation indicated that the impact on the results of RR assimilation was less sensitive to errors in the magnitude estimate than errors in the RR location.

5) It was shown that assimilation of *RR* only was not as effective in producing a satisfactory improvement on the cyclone prediction as the assimilation of both *PW* and *RR*. In addition, improvement in the cyclone prediction of *RR* assimilation was found to depend on the moist parameterization scheme since the Grell (1993) cumulus parameterization resulted in a better 24-h cyclone forecast than the Kuo convective parameterization.

These results show that the SSM/I-measured *PW* and *RR* have great potential to improve the initial conditions for a mesoscale model, especially over the data-sparse oceanic regions. The case study carried out in this paper shows that the variational assimilation of SSM/I-measured *PW* and *RR* data produces adjustments in the model states and results in a positive impact on the forecast of the ERICA IOP-4 cyclone. Future experimentation is planned to assimilate the brightness temperature directly into a mesoscale model.

## 1. Introduction

Since the advent of meteorological satellites in the 1960's, numerous experiments have been conducted to evaluate the impact of these data on atmospheric analysis and prediction. The earlier studies mainly focused on satellite images of cloud cover, which were used to improve analysis of pressure systems and fronts, and to make inferences of atmospheric stability, wind, moisture, and precipitation (Vaughan and Johnson 1994). Quantitative data from satellites began in the late 1960's and have substantially improved in accuracy in recent years. It is now widely recognized that satellite products have a positive impact on operational analysis and forecasts, especially in the data-sparse oceanic areas where conventional radiosonde measurements are not available.

Among all the observational data from satellites, microwave remote sensing sounding has been proven to be the most informative source of data to provide significant improvements in quantitative measurements of atmospheric variables (Stanley and Thomas 1995). The Special Sensor Microwave/Imager (SSM/I) that flies aboard the Defense Meteorological Satellite Program (DMSP) satellites is a seven-channel, four frequency, linear-polarized, passive microwave radiometric system which measures atmospheric, ocean and terrain microwave brightness temperatures at 19.35, 22.235, 37.0 and 85.5 GHz. All frequencies are received in dual polarization except 22.235 GHz, which is received in vertical polarization only. The active portion of the conical scan covers a swath of about 1400 km, and the geometric resolution of processed brightness temperatures is 25 km (except 85.5 GHz). Several atmospheric parameters can be retrieved from SSM/I observations (Hollinger 1991). Among them the total precipitable water (PW) and rain rate (RR) are of primary interest for numerical weather prediction (NWP). The impact of SSM/I-derived PW and RR, as additional sources of moisture information on numerical forecasting of tropical circulations (Ledvina and Pfaendtner 1995; Tsuyuki 1997), tropical cyclones and hurricanes (Shi et al. 1996; Peng and Chang 1996; Karyampudi et al. 1998) and mid-latitude rapid cyclogenesis (Chang et al. 1993; Manobianco et al. 1994; Chang and Holt 1994) have been investigated.



Assimilation of PW and RR is not as straightforward as that of the conventional wind, temperature and specific humidity data since both PW and RR are indirect model variables in two-dimensional (2D) space. Information on the vertical humidity structure must be constructed through a special retrieval algorithm while making use of PW and RR observations. For example, Haydu and Krishnamurti (1981) developed an analysis scheme to obtain a three-dimensional (3D) specific humidity field ( $q$ ) from PW (1000 to 500 hPa). They assumed an exponential decay of  $q$  with height, and the surface specific humidity was extrapolated upward under the constraint that its vertical integral must be equal to the calibrated PW. Another method to assimilate PW was proposed by Kuo et al. (1993), in which a linear correction was performed on the vertical  $q$  profile of a guess field obtained from a model under the constraint that the PW derived from the guess fields is equal to the observed  $PW$ . Iterations were performed to relax the model's  $PW$  toward the observed value while retaining the vertical structure of the model's humidity field. During the procedure, super-saturation was removed. However, both approaches contain *ad hoc* assumptions and do not weigh the information contained in the retrieval and the guess field in an optimal manner. Assimilation of RR, on the other hand, was conducted by either specifying the convective heating terms in the model's thermodynamic equations according to the observed RR (Fiorono and Warner 1981; Donner, 1988), or adjusting the vertical profile of temperature and moisture in such a way that the convective parameterization would produce an initially specified heating rate (Krishnamurti et al., 1984; Krishnamurti and Bedi, 1988). They all showed that an improved forecast could be obtained after incorporation of the observed rainfall rate.

Recently, another method, variational data assimilation, was explored by several authors for assimilation of  $PW$  and/or  $RR$ . Specifically, Kuo et al. (1996) assimilated the  $PW$  derived from analysis, Zupanski and Mesinger (1995) and Zou and Kuo (1996) assimilated the surface rainfall observations. They all presented positive impacts on quantitative precipitation forecast.

The variational approach (i) relaxes the need for various forms of "pre-processing" or "retrieval" operations, (ii) avoids attributing all the observed RR to convective type; and (iii) ensures obtaining a dynamically consistent initial condition (IC). In this paper, we will assess the impact of the variational assimilation of satellite-derived PW and RR on the prediction of a rapid extra-tropical cyclogenesis.

The effort to investigate rapid extra-tropical cyclogenesis, nicknamed "bomb", has been the focus of many research activities in the past decade (Reed et al., 1994). An outstanding example is the Experiment on Rapidly Intensifying Cyclones over the Atlantic (ERICA). Previous research has demonstrated that latent heat release is a major forcing mechanism for rapid cyclogenesis. For example, Kuo and Low-Nam (1990) showed that latent heating can account for nearly 50% of the rapid pressure falls. Accurate prediction of rapid cyclogenesis depends on accurate prediction of precipitation and its distribution, which in turn depends on the quality of the model initial condition. With the lack of data over the ocean, analyses of winds, temperature and water vapor are generally of poor quality. It would be highly desirable to examine the impact of satellite-derived *PW* and *RR* on moisture analysis and subsequent forecast. Chang et al. (1993) analyzed the SSM/I *PW* and *RR* of the ERICA IOP-4 case and compared them with *in situ* observations and model simulation. Chang and Holt (1994) assimilated the SSM/I *RR* data on the ERICA IOP-4 cyclone and showed a positive impact on cyclone prediction: A central pressure of 943 hPa was predicted in a 24-h forecast in which the SSM/I-derived *RR* data was incorporated, as compared with the prediction of a 952-hPa surface low in the control forecast without the use of *RR* observations. Assimilation of SSM/I *RR* in Chang and Holt's (1994) experiment was realized through a simple procedure which replaced the model convective heating rates with the SSM/I-measured *RR* within the SSM/I swath. Manobianco et al. (1994) also assimilated the satellite-derived *RR* into simulations of ERICA IOP-4 cyclone using the Goddard Mesoscale Atmospheric Simulation System (Kaplan et al. 1982; Karyampudi et al. 1988) and found that the positive impact of assimilating *RR* depends on the model

resolution, the use of the search algorithm, and the magnitude and position of RR. The assimilation technique used by Manobianco et al. (1994) does not require a priori partitioning of the precipitation into stratiform or convection components. Satellite-derived RRs at grid points where the model is not produced precipitation are also assimilated with a designed method using a search algorithm. In this paper, we perform a direct assimilation of both the SSM/I *RR* and *PW* data for the same case using adjoint techniques. Direct comparison between our results and theirs is not straightforward since the Penn State/NCAR mesoscale model version 5 (MM5) is used in this study, which is different from the NRL model used in Chang and Holt (1994). To help the interpretation of the results, however, we conduct an experiment using a similar convective heating replacement method with MM5. In this experiment, RR from the Kuo (1974) convective parameterization scheme is replaced with SSM/I-measured RR within the SSM/I swathes at 0000 UTC and 0930 UTC January 1989, with 3 hour and 6 hour forcing periods, respectively. The convective instability is checked at every time step during the forcing period as is required for the replacement. We will compare the results of the convective heating replacement with those using the adjoint technique.

The paper is arranged as follows. In section 2 we briefly describe the ERICA IOP-4 cyclone. Section 3 summarizes the methodology of deriving the *PW* and *RR* from SSM/I brightness temperature measurements. The MM5 model and its adjoint model, variational data assimilation formalism, and the experimental design are presented in section 3. Numerical results of the 3-dimensional and 4-dimensional variational data assimilation experiments are discussed in sections 4 and 5, respectively. The paper is concluded in section 6.

## **2. Synoptic Overview of the ERICA IOP-4 Cyclogenesis**

The ERICA IOP-4 storm was the most intense cyclone among the 8 cases studied during the ERICA experiment. The analysis of National Centers for Environmental Pre-

diction (NCEP) at 0000 UTC 4 January 1989 indicated a broadly distributed baroclinicity without sharp frontal structure (not shown). The incipient low was located over Cape Hatteras with a central pressure of 996 hPa. ERICA field summary, NCEP analysis, and the surface analysis by Neiman and Shapiro (1993), as well as air-borne radar observations presented in Wakimoto et al. (1992), showed that the low experienced an intense deepening and moved rapidly toward the east and northeast over the western North Atlantic Ocean. The NCEP global analysis indicated that the cyclone deepened 41 hPa in 24 hrs, while the surface analysis by Neiman and Shapiro (1993) suggested a deepening of 60 hPa in 24 hrs.

During the initial stages of the development, a coastal trough and front extended south-westward from the cyclone center, separating the warm, moist air over the Gulf Stream from cooler and drier continental air situated over the coastal plain. The low developed in response to a vigorous upper-level short wave that moved across the United States from the northwest and reached the east coast at approximately 0000 UTC 4 January 1989. After connecting with a fast-moving upper-level trough, the surface low rapidly developed into a very intense marine cyclone with central pressures of 974, 960, and 941 hPa at 0600, 1200, and 1800 UTC, respectively. The cyclone finally reached a minimum of 936 hPa with a maximum surface wind in excess of  $70 \text{ ms}^{-1}$  at 0000 UTC 5 January (Neiman Shapiro 1993).

During the rapid development of the ERICA IOP-4 cyclone, DMSP F-8 satellite with its SSM/I instrument happened to fly over the cyclone region at times around 0000, 0930, and 2200 UTC 4 January. Figure 1 depicts the over-passes of SSM/I at these three times, respectively. The dot points in Fig. 1 are the locations where observations of six channels' brightness temperatures (19.350V, 19.350H, 22.235V, 37.000V, 37.000H and 85.500H) are available. The *PW* and *RR* are then retrieved from the brightness temperature measurements. Also shown in Fig. 1 is the cyclone position and subjective frontal analysis at 0930 and 2200 UTC, which were linearly interpolated from the analyses of Neiman Shapiro

(1993). These frontal analyses are not performed based on surface observations and shall only serve as a reference. The SSM/I brightness temperature fields of 19.35 GHz in the vertical polarization (thin solid line) are overlaid to view the distribution of cloud features with respect to the frontal positions. The overlapping of the satellite over-passes with the cyclone provide us an ideal situation to assess the impact of SSM/I data on the simulation of the cyclogenesis.

### 3. Methodology

#### *a. Retrieval algorithms of PW and RR*

Total PW and RR were computed from DMSP SSM/I brightness temperature measurements. Most of the retrieval algorithms were either statistically or physically-statistically based. Following is a brief description of the statistical method used to calculate the SSM/I-measured PW and RR data used in our assimilation experiments.

The PW is calculated by the algorithm according to the nonlinear regression of Alshouse et al. (1990). This method is valid over open ocean regions and the accuracy over land is decreased. The algorithm was used because it has low root-mean-square error (RMSE) and it was widely used in the literature (Hollinger 1991). It is a regression based on a nonlinear combination of the brightness temperatures measured by the 19-GHz, 22.235-GHz, and 37-GHz channels:

$$PW = 232.89 - 0.148596T_{19V} - 1.829125T_{22V} - 0.36954T_{37V} + 0.006193T_{22V}^2, \quad (3.1)$$

where  $PW$  is in unit  $kg\ m^{-2}$ , and  $T_{19V}$ ,  $T_{22V}$ , and  $T_{37V}$  are the brightness temperatures at 19 GHz, 22.235 GHz and 37 GHz in vertical polarization. The nonlinearity in the regression arises from a quadratic term for the 22.235 GHz channel. According to Hollinger (1991), a precipitation screen has to be applied prior to computing  $PW$ . The precipitation screen which is based on the 37 GHz vertical and horizontal polarization channels is applied in

the computation of  $PW$  only when the following condition is satisfied:

$$-11.7939 - 0.02727T_{37V} + 0.09929T_{37H} \leq 0 \text{ K.} \quad (3.2)$$

The SSM/I RR algorithm was originally described by Olson (1989) and Hollinger (1991). Since the 85 GHz (V) channel was deemed unstable during ERICA, an alternative algorithm was applied by Chang et al. (1993) using 85 GHz (H) channel, as well as the 22.235 GHz (V), 37 GHz (V) and (H) channels, and 19 GHz (V) and (H) channels in their analysis. The following formulae were adopted to derive the SSM/I-measured RR:

$$RR = \exp(-0.42383 - 0.0082985T_{85H} + 0.01496T_{19V} + 0.00583T_{19H}) - 4.0 \text{ mm h}^{-1}, \quad (3.3)$$

over the ocean, and

$$RR = \exp(1.32526 - 0.08150T_{37V} + 0.01638T_{37H} + 0.03561T_{22V} + 0.05079T_{19V} - 0.01875T_{19H}) - 8.0 \text{ mm h}^{-1}, \quad (3.4)$$

over land, where  $RR$  is the rain rate in  $\text{mm h}^{-1}$  and  $T_{37V}$ ,  $T_{37H}$ ,  $T_{19V}$ ,  $T_{19H}$ ,  $T_{22V}$ , and  $T_{85H}$  are the brightness temperatures of the 37-GHz (V), 37-GHz (H), 19-GHz (V), 19-GHz (H), 22.235 GHz (V), and 85-GHz (H) channels, respectively.

As mentioned earlier, there were 3 passes of the DMSP F-8 satellite over the ERICA IOP-4 cyclone at about 0000, 0930 and 2200 UTC 4 January 1989. Brightness temperatures were sampled in the scan region which covered a swath of about 1400 Km with the geometric resolution of approximately 25 Km (except 85 GHz). The precipitable water (PW) and rainfall rate (RR) were retrieved at each pixel within the swath according to the algorithm described above and then bilinearly interpolated to the model grid points. Due to the poor accuracy, the retrieved  $PW$  over land is not included in the assimilation. The model domain for this study covers an area of about  $3550 \times 4450 \text{ Km}^2$  with the central latitude and longitude of  $41^\circ\text{N}$  and  $65^\circ\text{W}$ . Model forecasts were carried out after the data assimilation was completed.

### *b. Numerical forecasting model and its adjoint*

The numerical forecasting model used for this study is the Penn State/NCAR mesoscale model version 5 (MM5). MM5 is a limited-area, non-hydrostatic primitive equation model with multiple options of physical parameterization schemes (Dudhia 1993; Grell et al. 1994). It originated from the earlier hydrostatic mesoscale model (Anthes and Warner 1978). The version we used for this study includes a bulk aerodynamic planetary boundary-layer parameterization, surface friction, surface fluxes, dry convective adjustment, grid-resolvable scale precipitation, and a cumulus parameterization scheme developed by Grell (1993). The Dudhia's simple ice explicit moisture scheme is used to treat the grid-resolvable scale precipitation in the forward model forecast.

The MM5 adjoint model was developed according to the method proposed by Navon et al. (1992). Applications of the MM5 adjoint model to 4-dimensional variational data assimilation has been demonstrated in papers by Zou et al. (1995), Kuo et al. (1996) and Zou and Kuo (1996). A detailed description of the MM5 adjoint model system can be found in Zou et al. (1997). In this study, the forward MM5 model and the backward adjoint use the same set of model physics during assimilation. The gradient check suggested by Navon et al. (1992) is made before the assimilation procedure.

### *c. Variational data assimilation formalism*

The cost function  $J$  which is minimized with respect to model initial condition based on the SSM/I-derived PW and RR consists of two terms: the observation term  $J^o(X(t_0))$  and a simple background term  $J^b(X(t_0))$ , i. e.,

$$J(X(t_0)) = J^b(X(t_0)) + J^o(X(t_0)). \quad (3.5)$$

The background is defined by

$$J^b(X(t_0)) = \frac{1}{2} \{X(t_0) - X_b\}^T B^{-1} \{X(t_0) - X_b\} \quad (3.6)$$

where  $X(t_0)$  is the initial condition which includes initial wind ( $u, v, w$ ), temperature ( $T$ ), specific humidity ( $q$ ) and pressure perturbation ( $p'$ ) and  $X_b$  is the background information



with estimated error covariance  $B$ . In this study, the MM5 analysis is used as the simplest approximation to  $X_b$  and  $B$  is a simple diagonal matrix proportional to the inverse of the root-mean-square (rms) errors of the analysis.

The observation term of the cost function consists of

$$J^o(X(t_0)) = \frac{1}{2} \sum_{n=0}^N \left\{ [PW(t_i) - PW^{obs}(t_i)]^T W_{pw} [PW(t_i) - PW^{obs}(t_i)] \right. \\ \left. [RR(t_i) - RR^{obs}(t_i)]^T W_{rr} [RR(t_i) - RR^{obs}(t_i)] \right\}, \quad (3.7)$$

where  $PW(t_i)$  calculates the model predicted  $PW$  at time  $t_i$  and  $PW^{obs}(t_i)$  is SSM/I-observed  $PW$  at the same time.  $RR(t_i)$  represents the model predicted convective and stratiform  $RR$  at time  $t_i$  and  $RR^{obs}(t_i)$  is SSM/I-measured  $RR$  at the same time.  $N$  is the total number of observations available.  $W_{pw}$  and  $W_{rr}$  in (3.7) are the weightings for  $PW$ ,  $RR$  respectively. Here  $W_{pw}$  and  $W_{rr}$  are simply taken as  $30 \text{ kg}^{-2}/\text{m}^{-4}$  and  $10^6 \text{ mm}^{-2}/\text{h}^{-2}$  respectively, to make the two observation parts in (3.7) of similar magnitude at the zeroth iteration.

The  $RR(t_i)$  represents the total  $RR$  produced by the model moisture physics including not only the convective precipitation but also the grid-resolvable large scale precipitation. Some studies, such as Chang and Holt (1993), found that the convective precipitation is over 90% of the total precipitation in the Naval Research Laboratory limited-area model for this case. So they assumed that the satellite-derived precipitation was all convective in nature and forced the model to reproduce the observed precipitation through the convective parameterization. For MM5, our experiments show that convective precipitation is not always dominant in the total precipitation. Therefore, including both convective and grid-scale precipitation in (3.7) is more accurate than the method which simply replaces the model convective heating rate with the observed  $RR$ , without considering the contribution from grid-resolvable precipitation.

Model-predicted  $PW(t_i)$  in (3.7) is computed by integrating the vertical profile of  $q$



as follows:

$$PW = \frac{p^*}{g} \sum_{k=1}^{KX} q(k) \Delta\sigma(k), \quad (3.8)$$

where  $q(k)$  is the model specific humidity at the  $k$ -th layer,  $\Delta\sigma(k)$  the layer thickness of the model at the  $k$ -th layer,  $KX$  is the total number of layers, and  $p^*$  is defined as  $p_s - p_t$ , where  $p_s$  is the surface pressure, and  $p_t$  is the pressure at the top of the model (100 hPa).

The limited-memory quasi-Newton method of Liu and Nocedal (1989) was used to minimize the objective function in this study. With the model mesh size of  $65 \times 89 \times 16$ , the dimensions of the control variables is equal to 462,800. The background  $X_b$  is used as the initial guess to start the minimization procedure.

#### *d. Experimental design*

The impact of the SSM/I-derived PW and RR on the simulation of the cyclone development is assessed through a set of numerical experiments listed in Table 1 and 2. Fig. 1 shows the model domain used in our experiments. There are 16 vertical layers in the model. The model simulations are carried out at two meshes:  $65 \times 89$  and  $129 \times 177$  with a grid spacing of 50 km and 25 km, respectively. Initial conditions at 25-km resolution are obtained by a bilinear interpolation from the initial conditions at 50 km.

As summarized in Table 1, CTRC and CTRF, respectively, are coarse and fine-mesh control experiments, which start from the initial conditions of the MM5 analysis. Coarse-mesh experiment 3DVC assimilates the SSM/I-retrieved PW and RR at the initial time (0000 UTC), while 4DVC assimilates the PW and RR at both 0000 UTC and 0930 UTC. In fact, experiment 3DVC is a one-time step 4-dimensional variational data assimilation (4DVAR) and not a traditional 3DVAR. The assimilation window for the experiment 4DVC is 9.5 hours. The forecast experiments of 3DVC and 4DVC start from the optimal initial conditions obtained by minimizing a cost function which measures the distance between the model derived and observed PW and RR data at 0000 UTC and at times of both 0000 UTC and 0930 UTC, respectively. Experiments 3DVF and 4DVF are two fine-mesh model

forecasts at 25-*km* resolution based on the optimal initial conditions of 3DVC and 4DVC, respectively.

Table 2 summarizes a series of experiments which are performed in order to assess the sensitivity of *RR* assimilation to errors in the *RR* estimate, a different cumulus scheme and a different assimilation method. The *RR* assimilation experiments include data at both 0000 UTC and 0930 UTC. The model resolution in these experiments is 50 *km*.

Since the objective of this study is to assess the impact of variational assimilation of SSM/I *PW* and *RR* on the prediction of cyclogenesis, all the experiments are started at 0000 UTC 4 January and ended at 0000 UTC 5 January 1989. For experiments with a grid resolution of 50 *km*, a time step of 150 seconds is used. For experiments with a grid distance of 25 *km*, the time step is 75 seconds.

#### 4. Numerical Results of Data Assimilation

##### *a. Convergence*

The major challenges for the real data assimilation of SSM/I *PW* and *RR* data using MM5 are: (i) the SSM/I data do not necessarily cover the entire model domain; and (ii) the assimilation model may not represent the actual atmosphere well. Difficulties arising from these considerations are usually reflected in the convergence of the minimization and in the distribution of the "optimal" perturbation in the initial conditions.

Figure 2 shows the variations of the cost function with respect to the number of iterations during the minimization procedure for experiments 3DVC and 4DVC. Fifteen iterations were performed. The values of the cost function are reduced by one or two orders of magnitude in 10 to 15 iterations. This demonstrates that the minimization procedure of the MM5 adjoint system works well in experiments 3DVC and 4DVC. We will examine what modifications have been made to the initial guess field through these data assimilation procedures.

As was mentioned before, the first guess for experiments 3DVC and 4DVC are obtained from the NCEP analysis which enhanced with the radiosonde data at 0000 UTC 4 January 1989. Because of the sparsity of the radiosonde stations over the ocean, the first guess is inaccurate, especially off the east coast. Figure 3 presents the SSM/I-observed *PW* and *RR* at 0000 UTC, 0930 UTC and 2200 UTC 4 January 1989. These data are mostly available over the ocean, *i.e.* over the data-sparse regions. It is natural to expect that incorporation of these observations into the model will improve the quality of initial analysis at 0000 UTC 4 January 1989, which will result in a better forecast.

Indeed, the SSM/I-derived *PW* and *RR* observations have more detailed horizontal structure than the *PW* and *RR* fields in the model initial condition. As a comparison, we compute the *PW* based on the MM5 analysis (or first guess) at initial time (0000 UTC). The result is shown in Fig. 4a. Although the MM5 analysis-derived *PW* field (Fig. 4a) shows a similar pattern to the SSM/I observation (Fig. 3a), details are different. The area where *PW* is greater than 35 mm in the analysis is located to the southwest of the observed one. The *RR* at 0000 UTC in Fig. 4b is the *RR* of the model one-time-step integration. Due to the spin-up problem, MM5 does not produce much significant *RR* at initial time (Fig. 4b).

The *PW* and *RR* computed from the optimal initial conditions of 3DVC and 4DVC are shown in Figure 5. We find that after the data assimilation, the distributions of both *PW* and *RR* at 0000 UTC and 0930 UTC 4 January resemble the observations (Fig. 3) more than those of the control experiment (Fig. 4). The high *PW* regions at 0000 UTC tilt north-eastward in 3DVC and 4DVC compared to the original analysis. They are shifted to the northeast of their original moisture center in CTCR. The initial precipitation also occurs to the northeast of the original precipitation location in CTCR. The *RR* pattern at 0930 UTC in experiment 4DVC (Fig. 5f) looks very similar to the observation, especially the northern part of the rain band.

#### *b. Analysis of the optimal initial conditions*

Figure 6 shows the distribution of the sea level pressure and equivalent potential temperature at  $\sigma = 0.93$  at  $t=0$  h (0000 UTC 4 January) for experiments CTRC, 3DVC and 4DVC (Fig. 6a-c). As was mentioned, the CTRC starts from the MM5 analysis. There are two major differences between the original analysis and the "optimal" initial conditions. First, the MM5 analysis has a surface low center located on the east coast with a minimum pressure of 998 *hPa* (Fig. 6a), while the "optimal" initial conditions of both 3DVC and 4DVC produced the surface low center over the ocean, about 120 *km* to the east of the original center with a minimum pressure of 996 and 997 *hPa*, respectively (Fig. 6b and 6c). Compared with the analysis of Neiman and Shapiro (1993), the initial cyclone locations and intensities in experiments 3DVC and 4DVC are closer to the subjective analysis than that in CTRC. Analysis by Sanders (personal communication) also placed the cyclone center at 0000 UTC 4 January over the sea. The second distinct feature in the optimal initial conditions is found in the equivalent potential temperature field in the vicinity of the IOP-4 cyclone. A warm  $\theta_e$  anomaly was produced after the assimilation. Comparing Fig. 6b with Fig. 6c, it can be seen that experiment 3DVC which assimilated SSM/I *PW* and *RR* only at the initial time (0000 UTC), produced a stronger  $\theta_e$  anomaly than that of experiment 4DVC. This is because in 4DVC, observations at both times (0000 UTC and 0930 UTC) are assimilated. During the minimization procedure, the 4DVAR system must take into account the reductions of the cost function not only at 0000 UTC but also at 0930 UTC. Therefore, the fit to the observation at 0000 UTC is not as close as that of experiment 3DVC, which assimilated only the 0000 UTC observation. Modifications of the equivalent potential temperature field over southeastern part of the domain where the 0930 UTC observation is available are also found in the initial condition of 4DVC (see Fig. 6c).

The eastward shift of the initial surface low and the intensified thermal anomaly in the equivalent potential temperature over the ocean seen in the optimal initial conditions, suggest that important information about the temperature and moisture structure asso-

ciated with the incipient cyclone is contained in the SSM/I *PW* and *RR* observations. Assimilation of these indirect observations is very effective in improving the model's initial state. With the lack of traditional observations over the ocean off the east coast, the original analysis does not describe the initial state for the incipient cyclone properly.

In order to study how the SSM/I *PW* and *RR* data affect the "optimal" initial conditions and modify the cyclone initial position, we examine the difference fields of temperature, humidity, and wind between the original analysis and the "optimal" initial conditions. Figure 7 shows the cross-section of the temperature and humidity differences,  $\Delta T$  and  $\Delta q$ , between the 3DVC "optimal" initial condition and MM5 analysis along the line AB in Fig. 6b. We find that both the low-level temperature and humidity in the cyclone area are increased after assimilating observed *PW* and *RR*. Together, this creates a warm anomaly in the equivalent potential temperature field and a decrease in surface pressure. The experiment 4DVC also produces a similar modification in the cyclone area (Fig. 8). In addition, experiment 4DVC modified the temperature and humidity over the area where 0930 UTC observations are taken and caused the lower level temperature and humidity to increase in that area as well. These changes, however, are not necessarily realistic. In 4DVAR, observations at later times are used to modify the model state at the initial time. Adjustments in the initial conditions may also contain model errors. At present, we have no available observations at 0000 UTC to verify the increase of temperature and humidity to the east of  $70^{\circ}W$  (Fig. 8). But the modification in the initial conditions through 4DVAR approach reduces the prediction error. Another advantage is that the initial conditions generated by 4DVAR are model-consistent. Assimilation of both *PW* and *RR* (as useful sources of moisture information) can help lessening the "spin-up" problem which often exists in short-range numerical weather prediction.

## 5. Numerical Results of Model Forecast

### a. Control simulation

In order to assess the impact of SSM/I-measured  $PW$  and  $RR$  on the numerical forecast, the control experiment without assimilation is carried out to serve as a benchmark. The simulated sea level pressure and equivalent potential temperature fields at  $\sigma = 0.93$  at 0000 UTC 5 January 1989 are shown in Fig. 9a (CTRC) and b (CTRF). Experiment CTRC predicted a cyclone with a central pressure of 940  $hPa$  at 0000 UTC 5 January and CTRF predicted a cyclone of 935  $hPa$ . According to Neiman and Shapiro (1993) the cyclone deepened by 60  $hPa$  in 24 hours and reached 936  $hPa$  at 0000 UTC 5 January. Compared with the subjective analysis by Neiman and Shapiro (1993), CTRC predicted a slightly weaker cyclone, while CTRF predicted a slightly stronger cyclone. The simulated cyclone tracks are not very accurate in both experiments CTRC and CTRF. CTRC and CTRF, respectively, predict cyclone positions about 263  $km$  and 204  $km$  to the southeast of the analyzed location (see table 1). The simulated cyclone moves slower than that in the analysis. Increasing the model resolution improves the prediction of the cyclone intensity, but does little with respect to the cyclone track.

Figure 10 presents the model-predicted  $RR$  at 0930 UTC and 2200 UTC 4 January 1989, when the SSM/I-observed  $RR$  are available for verification. From Fig. 10 we see that experiment CTRC did not capture the observed rain band structure well both at 0930 UTC (Fig. 3d) and 2200 UTC (Fig. 3f). Because the control experiment CTRC did not predict the frontal position accurately, the precipitation along the cold and warm fronts is also misplaced. In fact, the simulated  $RR$  for the experiment CTRC at 0930 UTC in Fig. 10a is just on the edge of the observed SSM/I swath area. It falls behind the SSM/I-measured  $RR$  by approximately 250  $km$ . The prediction of  $RR$  at 2200 UTC (Fig. 10b) is even less accurate compared with the observed  $RR$  (Fig. 3f). No narrow rain band along the cold front was predicted at all.

Figure 11 shows the results of 25- $km$  grid control run CTRF. The overall pattern of predicted  $RR$  at 0930 UTC (Fig. 11a) is similar to that of experiment CTRC (Fig. 10a). The location is about 250  $km$  to the southeast of the observed location. The predicted

$RR$  in CTRF at 2200 UTC (Fig. 11b) is much improved over that of CTRC. The narrow rain band associated with the cold front appears in the simulated  $RR$  field at 2200 UTC, although it is not as well organized as that in the observed field. The position is still shifted to the west of the observed rain band. This is consistent with the lag of the simulated cyclone and its associated fronts in the control experiments. Increasing the model resolution does not remedy the problem of the slow movement of the predicted IOP-4 cyclone.

*b. 50-Km simulations from "optimal" initial conditions*

The sea level pressure and equivalent potential temperature fields at  $\sigma = 0.93$  for experiments 3DVC and 4DVC at 0000 UTC 5 January 1989 are shown in Fig. 12a and 12b, respectively. The predicted cyclone positions at 0000 UTC 5 January in both 3DVC and 4DVC are located closer to the observed position analyzed by Neiman and Shapiro (1993) (see Fig. 3 in their paper). 4DVC did a better job than 3DVC. Note that 4DVC was able to move the cold front further to the east, consistent with the observation. As far as the frontal structure of the cyclone is concerned, both 3DVC and 4DVC did equally well. Distinct cold and warm frontal zone in the equivalent potential temperature field are produced. As a matter of fact, the frontal structure is also quite good in the control experiment (Fig. 9). The major improvement produced by 4DVC over 3DVC and CTRC is the frontal position. Because the precipitation is usually related to the front, we expect that the improved frontal position will result in a better prediction of rainfall pattern.

Examining model predicted  $RR$  distributions at 0930 UTC and 2200 UTC for 3DVC (Fig. 13), we find that experiment 3DVC does not capture the structure of  $RR$  at both 0930 UTC and 2200 UTC very well, although the amount of  $RR$  is larger than that of CTRC (Fig. 10). As was mentioned, the observed  $RR$  at 0930 UTC and 2200 UTC (Fig. 3) displays a distinct line structure corresponding to the cold and warm fronts. Such a structure is not produced in 3DVC. On the other hand, 4DVC produces corresponding  $RR$  pattern after data assimilation at 0930 UTC (Fig. 5f) similar to that of the observation.

The simulated cold frontal rain band at 2200 UTC in 4DVC (Fig. 14) resembles the observed *RR* more than that of CTRC and 3DVC (Fig. 10b and Fig. 13b). The rain band related to the cold front is captured distinctively, although not all the rain cell along the cold front is simulated well. For example, the rain cell in the middle of the narrow band is not predicted well. These results show that the 4-dimensional variational data assimilation experiment 4DVC produces better results not only in the cyclone movement, but also in the *RR* prediction.

In seeking the reasons why 4DVC did a better job than 3DVC, we examine the distribution of the moisture convergence and the vertical velocity distributions in the two experiments. Figure 15 shows the distribution of moisture convergence at 850-hPa level at 1200 UTC 4 and 0000 UTC 5 January for 3DVC (Fig. 15a,c) and 4DVC (Fig. 15b,d), respectively. A noticeable feature in the moisture convergence is that a clearly defined T-bone shaped moisture convergence (dashed lines) associated with warm and cold fronts is observed at 1200 UTC 4 January in 4DVC, but not clearly defined in 3DVC. The moisture convergence associated with the warm front (oriented from west to east) of 4DVC also extends further to the north than that in 3DVC. At 0000 UTC 5 January, the moisture convergence associated with the cold front appears in 4DVC (Fig. 15d), but is missing in 3DVAR (Fig. 15c). The structure of the moisture divergence behind the cold front is also different in the two simulations. The maximum moisture convergence associated with the warm front in 4DVC is located to the northeast of that of 3DVC. Such a difference in the mesoscale structure of the moisture convergence is reflected also in the vertical velocity fields (Fig. 16) at 500 hPa. The vertical velocity in 3DVC at 500 hPa presents a half circular pattern (Fig. 16a) at 1200 UTC 4 January, while that in 4DVC (Fig. 16b) shows a distinct T-bone pattern. Similarly, at 0000 UTC 5 January, large vertical velocity is observed only in the warm front region in 3DVC (Fig. 16c) but not in the cold front region, where a line of upward vertical motion is predicted by 4DVC (Fig. 16d).

The main differences between 3DVC and 4DVC are that in 4DVC the satellite-derived



RR and PW data at 0930 UTC 4 January are incorporated into the assimilation and the model is being used as a strong dynamic constraint between the two observation times (0000 UTC and 0930 UTC 4 January). Differences in the model initial conditions due to the assimilation of observations at 0930 UTC remain visible in the subsequent forecast. The adjustments in the initial conditions in 4DVC is more beneficial to the forecast than that in 3DVC.

In order to see exactly how the cyclone tracks differ in the three 50-km forecast experiments, the cyclone positions at 6-h intervals from 0000 UTC 4 to 0000 UTC 5 January are plotted in Fig. 17. The observed cyclone position as analyzed by Neiman and Shapiro (1993) is also plotted in the figure. It can be seen that the best forecast of cyclone track is obtained from experiment 4DVC, the second best is the 3DVC and the worst is the control experiment CTRC without assimilation. The control experiment CTRC starting with a misplaced surface low in the initial condition predicts the cyclone movement more slowly than that of experiments 3DVC and 4DVC. For experiments 3DVC and 4DVC, although the cyclone position in the "optimal" initial analysis is not perfect, the cyclone center is indeed located over the ocean, consistent with the post-ERICA analysis. In the subsequent forecast, experiment 4DVC produces the best cyclone track prediction. At 0000 UTC 5 January, the predicted cyclone position by 4DVC is only about 42 km (less than 1 grid distance) off from the observed location (see Table 1). This demonstrates a great potential for the 4D-variational assimilation of *PW* and *RR* for ocean cyclone prediction.

Figures 18a and b show 850-hPa temperature and wind fields at 0000 UTC 5 January 1989 for both CTRC and 4DVC. At 0000 UTC 5 January, 850-hPa wind vectors distribution reflects that the cyclone is located more northward in 4DVC than in CTRC. This is consistent with the predicted surface fields in Fig. 12b. Examining the 850-hPa temperature fields, both CTRC (Fig. 18a) and 4DVC (Fig. 18b) simulate the warm-core seclusion structure (Kuo, Reed and Low-Nam 1992). However, CTRC simulates a warm-core that is too strong, with its position lagged, compared with the analysis of Fig. 3d in Neiman,

Shapiro and Fedor (1993). On the contrary, 4DVC simulates the warm-core seclusion with more accurate intensity and position (compared with Fig. 3d in Neiman, Shapiro and Fedor 1993). The warm front is located further to the north in 4DVC (Fig. 18b) than in CTRC (Fig. 18a). Therefore, the improvement in the cyclone prediction as a result of assimilation of 0000 UTC and 0930 UTC *PW* and *RR* in experiment 4DVC is visible not only near the surface, but also in the lower troposphere.

The differences of the 700- and 500-hPa latent heating between the 4DVC and CTRC runs at 0000 UTC 5 January are shown in Figs. 18c and 18d, respectively. The positive pattern of 700- and 500-hPa heating differences (Figs. 18c,d) originated southwest to northeast along the cold front is due to the assimilation of *PW* and *RR*, which has shifted the heating eastward in the 4DVC run. In the vicinity of the low center, the assimilation experiment in 4DVC decreases the 700-hPa and 500-hPa latent heating as indicated by the negative differences. The latent heating differences between the 4DVC and CTRC at 1800 UTC 4 January are also presented negative pattern in the vicinity of the cyclone center (figure omitted). This means that the latent heat warming in 4DVC is slightly removed from the cyclone center due to the *PW* and *RR* assimilation than that in CTRC, in which it remains close to the cyclone center. Examining the temperature fields in Figs. 18a and 18b, we find that the low center in CTRC at 850 hPa (Fig. 18a) is warmer than that in 4DVC (Fig. 18b). Therefore, the 4-dimensional assimilation experiment 4DVC predicted a slightly weaker cyclone than CTRC in our case.

Experience with the cyclone prediction indicates that in addition to the initial condition which is most important to successful simulations of cyclones, another important factor is the horizontal resolution of the numerical model (Kuo and Low-Nam 1990; Manobianco et al. 1994). An intense deepening of the cyclone usually occurs when a finer grid mesh is used in the simulation. Such experiments are carried out in the following subsection.

### *c. 25-Km simulations from "optimal" initial conditions*

To assess the effects of horizontal resolution, two additional model forecasts, 3DVF and 4DVF, were conducted. These experiments are equivalent to 3DVC and 4DVC except the horizontal resolution which is changed from 50 km to 25 km. The initial conditions of the experiments 3DVF and 4DVF are obtained through a bilinear interpolation procedure on the optimal initial conditions of experiments 3DVC and 4DVC.

The simulated cyclone tracks at 25-*km* resolution are plotted in Fig. 19. It can be seen that the cyclone tracks in 3DVF and 4DVF are similar to 3DVC and 4DVC (Fig. 17) but slightly improved. The 24-h forecast error of the cyclone position by 4DVF is less than 30 *km* (Fig. 19 and table 1). More importantly, the fine mesh experiment 4DVF predicts the best temporal variation of cyclone intensity during the 24 h simulation, which is shown in Fig. 20. Furthermore, the experiment 4DVF with a grid distance of 25 *km* gives a much better cyclone intensity prediction than the coarse grid mesh 4DVC, especially during the second 12 hours of simulation (Fig. 20). At 0000 UTC 5 January, the fine grid experiment 4DVF predicts a cyclone with an intensity of 936 *hPa*, the same as the observed value.

In summary, 4DVF performs the best among all the experiments presented in this study. It produces not only a good cyclone track, but also a perfect intensity forecast at 0000 UTC 5 January (table 1). This experiment assimilated SSM/I-measured *PW* and *RR* at two time levels with a coarse resolution (50 *km*), and then used a fine grid mesh (25 *km*) for the forward 24-h forecast. This implies that one can use a simpler model with a coarse grid mesh in the assimilation to reduce the computing expense and then use a more sophisticated model with a finer grid mesh for the model forecast. This strategy worked well in the ERICA IOP-4 case, as was shown in Kuo et al. (1997).

#### *d. Some discussions on adjoint approach*

The variational assimilation of SSM/I *PW* and *RR* for ERICA IOP-4 is a new effort to assess the impact of these satellite data on cyclone prediction. This method assimilates the SSM/I observations at different time levels in a consistent manner into the initial

conditions. The modifications to the model initial state are produced through an adjoint operator applied to the differences between the simulated and the observed variables (*PW* and/or *RR*).

The spin-up problem has been the focus of numerous studies for more than a decade. It can be defined as a deficiency in the model's precipitation forecast within the first several hours of integration. Our results indicate that the initial condition based on the conventional data by the MM5 pre-processing system has insufficient moisture information and insufficient mesoscale details about vertical velocity, upper-level and low-level divergences and etc., especially over the ocean area due to the sparsity of the conventional radiosonde data. This poor initial conditions causes the model to underestimate the precipitation at the beginning of the model simulation. The weak precipitation then degrades the forecast due to the insufficient latent heat release. From Fig. 21a, for example, it can be seen that the total 3-h precipitation of control simulation CTRC in the cyclone area has a maximum of 5.89 mm. On the contrary, all the experiments starting from the "optimal" initial conditions (Fig. 21b,c) produce an amount of more than 35 mm in the first three hours of simulation, much larger than the control run CTRC. After assimilation of the *PW* and *RR*, the model initial conditions, especially the moisture fields, are modified under the model constraint during the optimal procedure of the variational approach. The model is able to predict a realistic amount of precipitation in the first few hours of the integration, which produces a positive impact on the subsequent forecast.

## 6. Rainfall Rate Assimilation Experiments: Sensitivity

Because different rainfall algorithms may yield different *RR* magnitudes and distributions, experiments A-E are designed to assess the impact of errors in the *RR* estimates as summarized in Table 2. Again CTRC in Table 1, a forecast run without data assimilation, is taken as a benchmark. Experiment A in Table 2 is an assimilation experiment in which the retrieved full *RR* are assimilated into forecast. For experiments B, C and D, system-

atic errors of -10%, -20% and -40% were introduced at both 0000UTC and 0930UTC to emulate the possible underestimates in SSM/I-retrieved *RR* due to sensor, data sampling, and algorithm errors. Experiment E is identical to experiment A except that the *RR* data is shifted 300 km to the west of the observed. The 300-km location error for precipitation is of course a gross exaggeration of any possible geodetic or geographic location errors of the observing system. From experiment A, it can be seen that the assimilation of SSM/I-retrieved *RR* improved the 24-h forecast of the cyclone position. The position error which was 263 km in CTRC, is now decreased to 185 km in experiment A (Table 2). When the *RR* magnitudes are reduced (experiments B-D), the improvement in the prediction of the cyclone position is not as large as with the *RR* assimilation experiment A. When the *RR* observation is misplaced (Experiment E), the 24-h cyclone position forecast shows no improvement. However, analysis of the 24-h cyclone intensities shows some mixed results. The reduction of *RR* magnitude slightly increases the cyclone intensity. In fact, even our control experiment without data assimilation produced a cyclone intensity (940 hPa) close to the observation. We will examine the impact of *RR* assimilation on the forecast of cyclone intensity and track further by comparing the RMS differences between the assimilation experiments and control run.

Figure 22 shows the RMS differences in the sea-level pressures between experiments A, B, C, D, or E and experiment CTRC in Table 1. Such a distribution of RMS differences reflects the sensitivity of *RR* assimilation to the accuracy and location of the *RR* observations. It can be seen that the modification is the largest when the full *RR* is assimilated. The less the *RR* is incorporated, the less the modification is. Assuming that assimilation of the full *RR* yields the largest modification (solid line in Fig.22), then the impact in assimilating SSM/I *RR* can be judged by the gap between the solid line in Fig. 22 and non-solid lines corresponding to the other experiments. The impact on the cyclone forecast as a result of *RR* assimilation decreases as the *RR* error increases. Experiment E which shifts the *RR* location produces the largest impact on the 24-hour forecast. How-

ever, the impacts are not uniform during the 24-h simulations. Based on Figure 22, the impact on cyclone forecast is not quite sensitive to the  $RR$  magnitude estimates during the assimilation period (0000-0930UTC). But it becomes more sensitive after 0930UTC. With regard to the  $RR$  location, the impact is sensitive even in the period of 0600-0930 UTC and becomes more sensitive after 0930 UTC. Figure 22 shows that a misposition of 300 km in  $RR$  causes a bigger impact on the 24-h cyclone forecast than 40%  $RR$  error in magnitude.

Experiments F and G in Table 2, respectively, are similar to experiment CTRC in Table 1 and experiment A in Table 2 except the Kuo cumulus parameterization scheme is used instead of the Grell (1993) scheme. We know that the extra-tropical storm forecast is sensitive to the cumulus parameterization scheme in the model (see Kuo et al. 1996). This is true also in the assimilation experiment (compare G with A). With the Grell (1993) cumulus parameterization scheme, assimilation of SSM/I-derived  $RR$  improves the 24-h cyclone intensity forecast from 940 hPa to 938 hPa and reduces the 24-h position error from 263 km to 185 km. With the Kuo scheme, assimilation of the  $RR$  reduces the 24-h position error from 263 km to 213 km without much improvement in intensity. From these two experiments (F and G), it is concluded that the Grell cumulus parameterization scheme (Grell 1993) performs better for the  $RR$  assimilation when PSU/NCAR MM5 is used in the forecast of this extra-tropical cyclone.

We also conducted experiment H using a different assimilation method (heating replacement method). As Chang and Holt (1994), we assumed the convective precipitation dominates the total precipitation and hence we replaced the model predicted latent heating from Kuo (1974) convective parameterization with the specified heating from the SSM/I rain rates. In the Kuo convective parameterization scheme, the rainfall rate ( $RR$ ) is proportional to the moisture convergence within the unit column, such that

$$RR = (1 - b)M_t, \quad (6.1)$$

where

$$M_t = -\frac{1}{g} \int_0^1 \nabla \cdot p^* \vec{V} q_v d\sigma \quad (6.2)$$

is the moisture convergence and  $b$  is a function of the mean relative humidity. The vertical heating profile is then specified as

$$\frac{\partial T}{\partial t} |_{con} = \frac{L_v}{C_p} N_h(\sigma) (1 - b) g M_t, \quad (6.3)$$

where  $N_h(\sigma)$  is the vertical distribution function of convective heating. In Experiment H, we made a numerical forecast by incorporating the *RR* at 0000 UTC and 0930 UTC 4 January. The *RR* at 0000 UTC 4 January were incorporated into MM5 over a 3-hour assimilation window from 0000 UTC to 0300 UTC 4 January, whereas *RR* at 0930 UTC 4 January were incorporated over a 6-hour assimilation window from 0630 UTC to 1230 UTC 4 January. The model-computed rainfall rates within the SSM/I swath were repeatedly replaced by the SSM/I rainfall rate in the assimilation windows. The convective instability in the column was checked at every time step as required when SSM/I-observed rainfall rate were assimilated. The 24-h forecast of either cyclone intensity or position showed no significant improvement compared to experiment F which did not assimilate *RR*.

It is interesting to make a comparison among experiment 4DVC in Table 1, and experiments A, G and H in Table 2. All of these experiments are 4-dimensional data assimilation experiments. As far as the cyclone position forecast is concerned, experiment H performs the worst and 4DVC the best. This leads to the following findings. First, 4DVAR assimilation of *RR* produces a slightly better forecast than the heating replacement method using MM5 for the ERICA IOP-4 cyclone. Second, Grell (1993) cumulus parameterization performs better than the Kuo scheme in our 4DVAR experiments of *RR* assimilation. Third, assimilating *RR* in itself is not sufficient to improve the forecast of the cyclone track. After *PW* is also included in the assimilation, the forecast of the cyclone track is much improved and the position error is reduced to less than 50 km.

## 7. Conclusions and Discussion

This paper examines the impact of variational assimilation of the SSM/I-retrieved *PW* and *RR* on the 24-hour numerical simulations of the ERICA IOP-4 cyclone initialized at 0000 UTC 4 January 1989. Numerical forecasts are performed at two resolutions (50 *km* and 25 *km*) with 16 layers in the vertical using the Penn State/NCAR MM5 model. Data assimilation experiments are performed only on the 50-*km* grid using adjoint techniques. The advantage of this approach is that it is not necessary to pre-specify the vertical structure of humidity to assimilate the two dimensional *PW*, or to specify a vertical latent heating based on the observed *RR*. Our findings are summarized as follows:

1) The MM5 adjoint system and the minimization procedure successfully assimilate the SSM/I-measured *PW* and *RR* into the MM5 model. This variational assimilation approach does not create large gradients along the boundaries of the swath in the model fields during or after the data assimilation period. Specifically, *PW* and *RR* assimilation do not produce additional gravity wave noises compared with those in the control experiments. Furthermore, the technique retrieves a dynamically consistent "optimal" initial condition of the ERICA IOP-4 cyclone. Minimization of the cost function is able to adjust the model initial condition in such a way that the model *PW* and *RR* are closer to observations.

2) After variational data assimilation, the "optimal" initial condition places the incipient cyclone over the ocean, about 120 *km* off the east coast of the United States, while the original analysis places it on the east coast. Compared with the post-ERICA subjective analysis by Neiman and Shapiro (1993), the "optimal" initial condition is more realistic than the original analysis. This shows that the SSM/I-measured *PW* and *RR* data contain useful information for cyclone prediction, especially over the ocean where no conventional rawinsonde observations are available.

3) Numerical results indicate that the forecasts initialized with the optimal initial conditions are improved. The improvements are reflected not only in the prediction of the cyclone tracks but also in the prediction of rainfall. The spin-up problem is greatly reduced in experiments with *PW* and *RR* assimilation.



4) Further improvement on the cyclone intensity forecast as a result of *PW* and *RR* assimilation is obtained when the horizontal resolution is increased from 50 *km* to 25 *km*. The impact of data assimilation on cyclone intensity forecast is small using a 50-*km* forecast model.

5) Sensitivity experiments on *RR* assimilation show that the results from variational experiments are not very sensitive to errors in the *RR* estimate during the assimilation period (0000-0930UTC). But sensitivity increases during the forecast after assimilation. The cyclone forecast is more sensitive to errors in *RR* position than errors in retrieved *RR* magnitude. The *RR* assimilation experiments are also sensitive to cumulus parameterization schemes. The Grell (1993) cumulus parameterization performs better than the Kuo scheme in our 4DVAR experiments of *RR* assimilation with MM5 and MM5 adjoint systems for this ERICA IOP-4 cyclone case.

6) It is tested that variational assimilation of *RR* in itself is not sufficient to produce a satisfactory improvement on the cyclone prediction for the ERICA IOP-4 case. The experiment incorporating both SSM/I-derived *PW* and *RR* results in a significant improvement in the cyclone forecast, especially the cyclone track prediction.

These results show that the SSM/I-derived *PW* and *RR* have great potential for improving cyclone prediction. The sensitivity of the numerical results of the variational assimilation approach to errors in satellite *RR* is consistent with that of Chang and Holt (1994) and Manobianco et al. (1994), that is, the assimilation of *RR* is less sensitive to the errors in magnitude but more sensitive to the error in location. By comparing our results with those of Chang and Holt (1994) and Manobianco et al. (1994), the impact of assimilating satellite *RR* on the simulations of IOP-4 cyclone appears to depend on the relative accuracy of the control run, which to a large extent depends on the sophistication of the model, particularly improved physics. Chang and Holt (1994) found that *RR* assimilation had a significant impact on the intensity of the cyclone compared to their control run, which predicted a significantly weak cyclone. Our results that *RR* assimilation had a large

impact on cyclone and frontal locations and a small impact on cyclone intensity, confirm the findings of Manobianco et al. (1994), who also found that increasing the horizontal resolution decreased the intensity errors similar to the results from this study.

Recently, Karyampudi et al. (1998) found that RR assimilation is sensitive to cumulus parameterization scheme. Within the framework of variational method, we obtained a similar conclusion. However, assimilation of RR with the heating replacement method in this study shows no significant improvement in the 24-h forecast of either cyclone intensity or position. This may be attributed to the use of a fixed-parabolic heating profile in the Kuo scheme of MM5 (Grell et al. 1994), in contrast to the original Kuo scheme used in the study of Chang and Holt (1994). Karyampudi et al. (1998) found that a fixed profile with upper-level heating maximum underestimates cyclonic development and is not adequate to describe the rapid development with mid-level heating maximum. Therefore, the simulations with the Kuo scheme in MM5 which has upper-level heating maximum are not as good as those of Chang and Holt (1994) as well as those from the Grell cumulus parameterization scheme.

The variational assimilation method allows a direct assimilation of the SSM/I brightness temperatures, instead of their retrieval products (such as PW and RR). Our next step is to assimilate the SSM/I brightness temperatures which are the rawer form of the SSM/I observations and to examine the advantages and disadvantages of assimilating the brightness temperatures versus the retrieval products. Direct assimilation of SSM/I brightness temperatures can avoid errors both in the background information (used for the retrieval) and in the retrieval procedure.

*Acknowledgments.* We express our great appreciation to Dr. Simon Chang of Navy Research Laboratory for providing us with the SSM/I data. We also gratefully acknowledge the anonymous reviewers, whose comments and suggestions have greatly improved the presentation of the paper. This research is supported by AFOSR through project number

## REFERENCES

- Alishouse, J., S. Snyder, J. Vongsathorn, and E. Ferraro, 1990: Determinations of oceanic total precipitable water from the SSM/I, *IEEE Trans. Geosci. Remote Sens.*, **28**, 811-816.
- Anthes, R. A., and T. T. Warner, 1978: Development of hydrodynamic models suitable for air pollution and other meso-meteorological studies. *Mon. Wea. Rev.*, **106**, 1045-1078.
- Chang, S. W., R. J. Alliss, S. Raman, and J. J. Shi, 1993: SSM/I observations of ERICA IOP-4 marine cyclone: A comparison with in situ observations and model simulation. *Mon. Wea. Rev.*, **121**, 2452-2464.
- Chang, S. W., and T. R. Holt, 1994: Impact of assimilating SSM/I rainfall rates on numerical prediction of winter cyclones. *Mon. Wea. Rev.*, **122**, 151-164.
- Donner, L. J., 1988: An initialization for cumulus convection in numerical weather prediction models. *Mon. Wea. Rev.*, **116**, 377-385.
- Dudhia, J., 1993: A non-hydrostatic version of the Penn State-NCAR mesoscale model: Validation tests and simulation of an Atlantic cyclone and cold front. *Mon. Wea. Rev.* **121**, 1493-1513.
- Fiorino, M., and T. T. Warner, 1981: Incorporating surface winds and rainfall rates into the initialization of a mesoscale hurricane model. *Mon. Wea. Rev.*, **109**, 1914-1929.
- Grell, G. A., 1993: Prognostic evaluation of assumptions used by cumulus parameterizations. *Mon. Wea. Rev.*, **121**, 764-787.
- Grell, G. A., J. Dudhia, and D. R. Stauffer, 1994: A description of the fifth-generation

- Penn State/NCAR mesoscale model (MM5). *NCAR Technical Note*, NCAR/TN-398 + STR, National Center for Atmospheric Research, Boulder, CO, 138 pp.
- Haydu, K. J., and N. Krishnamurti, 1981: Moisture analysis from radiosonde and microwave spectrometer data. *J. Appl. Meteor.*, **20**, 1177-1191.
- Hollinger, J. P., 1991: DMSP Special Sensor Microwave/Imager calibration/Validation. *Final Report Vol.II*, Naval Research Laboratory, Washington, D. C., 6-39.
- Holton, J. R., 1992: An Introduction to Dynamic Meteorology, Third Edition, 80-81, *Academic press*, 511pp.
- Kaplan, M. L., J. W. Zack, V. C. Wong, and J. J. Tuccillo, 1982: Initial results from a mesoscale atmospheric simulation system and comparisons with the AVE-SESAME I data set. *Mon. Wea. Rev.*, **110**, 1564-1590.
- Karyampudi, V. M., G. S. Lai, and J. Manobianco, 1998: Impact of initial conditions, rainfall assimilation, and cumulus parameterization on simulations of Hurricane Florence (1988). *Mon. Wea. Rev.*, **126**, 3077-3101.
- Karyampudi, V. M., J. W. Zack, M. L. Kaplan, and J. M. Gram, 1988: A split-explicit time integration scheme for the MASS model. Preprints, *Eighth Conf. on Numerical Weather Prediction*. Baltimore, MD, Amer. Meteor. Soc., 807-814.
- Krishnamurti, T. N., K. Ingles, S. Cocke, R. Pasch, and T. Kitade, 1984: Details of low latitude medium-range numerical weather prediction using a global spectra model. Part II: Effects of orography and physical initialization. *J. Meteor. Soc. Japan*, **62**, 613-649.
- Krishnamurti, T. N., and H. S. Bedi, 1988: Cumulus parameterization and rainfall rates III. *Mon. Wea. Rev.*, **116**, 583-599.
- Kuo, Y.-H. and S. Low-Nam, 1990: Prediction of nine explosive cyclones over the western

- Atlantic Ocean with a regional model. *Mon. Wea. Rev.* **118**, 3-25.
- Kuo, Y.-H., Y.-R. Guo, and E. R. Westwater, 1993: Assimilation of precipitable water measurements into a mesoscale numerical model. *Mon. Wea. Rev.* **121**, 1215-1238.
- Kuo, Y.-H., X. Zou, and Y.-R. Guo, 1996: Variational assimilation of precipitable water using a nonhydrostatic mesoscale adjoint model. Part I: Moisture retrieval and sensitivity experiments. *Mon. Wea. Rev.*, **124**, 122-147.
- Kuo, Y.-H., R. Reed, and Y. Liu, 1996: The ERICA IOP5 storm. Part III: Mesoscale cyclogenesis and precipitation parameterization, *Mon. Wea. Rev.*, **124**, 1409-1434.
- Kuo, Y.-H., R. Reed, and S. Low-Nam, 1992: Thermal structure and airflow in the model simulation of an occluded marine cyclone. *Mon. Wea. Rev.*, **120**, 2280-2297.
- Kuo, Y.-H., X. Zou, and W. Huang, 1997: The impact of global positioning system data on the prediction of an extratropical cyclone: an observing system simulation experiment. *Dynamics of Atmospheres and Oceans*, **27**, 439-470.
- Ledvina, D. V., and J. Pfaendtner, 1995: Inclusion of Special Sensor Microwave/Imager (SSM/I) total precipitable water estimates into the GOES-1 data assimilation system. *Mon. Wea. Rev.*, **123**, 3003-3015.
- Liu, D. C., and J. Nocedal, 1989: On the limited memory BFGS method for large scale optimization. *Mathematical Programming*, **45**, 503-528.
- Manobianco, J., S. Koch, V. M. Karyampudi, and A. J. Negri, 1994: The impact of assimilating satellite-derived precipitation rates on numerical simulations of the ERICA IOP-4 cyclone. *Mon. Wea. Rev.*, **122**, 341-365.
- Navon, I. M., X. Zou, J. Derber, and J. Sela, 1992: Variational data assimilation with an adiabatic version of the NMC spectral model. *Mon. Wea. Rev.*, **120**, 1433-1446.
- Neiman, P. J. and M. A. Shapiro, 1993: The life cycle of an extratropical marine cyclone.

Part I: Frontal-cyclone evolution and thermodynamic air-sea interaction, *Mon. Wea. Rev.*, **121**, 2153-2176

Neiman, P. J., M. A. Shapiro, and L. S. Fedor, 1993: The life cycle of an extratropical marine cyclone. Part II: Mesoscale structure and diagnostics. *Mon. Wea. Rev.*, **121**, 2177-2199.

Olson, W. S., 1989: Physical retrieval of rainfall rates over the ocean by multispectral microwave radiometry-application to tropical cyclones. *J. Geophys. Res.*, **94**, 2267-2280.

Peng, M. S., and S. W. Chang, 1996: Impacts of SSM/I-retrieved rainfall rates on numerical precipitation of a tropical cyclone. *Mon. Wea. Rev.*, **124**, 1181-1198.

Reed, R., Y.-H. Kuo and S. Low-Nam, 1994: An adiabatic simulation of the ERICA IOP4 storm: An example of quasi-ideal frontal cyclone development. *Mon. Wea. Rev.*, **122**, 2688-2708.

Shi, J. J., S. W. Chang, and S. Raman, 1996: Impact on assimilations of dropsonde data and SSM/I rain rates on numerical prediction of Hurricane Florence (1988). *Mon. Wea. Rev.*, **124**, 1435-1448.

Stanley, Q. K., and H. V. H. Thomas, 1995: Satellite Meteorology - An Introduction, *Academic Press*, 466pp.

Tsuyuki, T. 1997: Variational data assimilation in the tropics using precipitation data. Part III: Assimilation of SSM/I precipitation rates. *Mon. Wea. Rev.*, **125**, 1447-1464.

Vaughan W. W. and D. L. Johnson, 1994: Meteorological satellites - The very early years prior to the launch of TIROS-1. *Bull. Amer. Met. Soc.*, **75**, 2295-2302.

Wakimoto, R., W. Blier, and C. Liu, 1992: The frontal structure of an explosive oceanic

- cyclone: Airborne radar observations of ERICA IOP 4. *Mon. Wea. Rev.*, **120**, 1135-1155.
- Zou, X., and Y.-H. Kuo, 1996: Rainfall assimilation through an optimal control of initial and boundary conditions in a limited-area mesoscale model. *Mon. Wea. Rev.*, **124**, 2859-2882.
- Zou, X., Y.-H. Kuo, and Y.-R. Guo, 1995: Assimilation of atmospheric radio refractivity using a non-hydrostatic adjoint model. *Mon. Wea. Rev.*, **123**, 2229-2249.
- Zou, X., F. Vandenberghe, M. Pondeva, and Y.-H. Kuo, 1997: Introduction to Adjoint Techniques and the MM5 Adjoint Modeling System. *NCAR Technical Note*, NCAR/TN-435 - STR, National Center for Atmospheric Research, Boulder, CO, 110pp.
- Zupanski, D. and F. Mesinger, 1995: Four-dimensional variational assimilation of precipitation data. *Mon. Wea. Rev.*, **123**, 1112-1127.

### Caption

Table 1: SSM/I precipitable water and rainfall rate assimilation experiments.

Table 2: SSM/I rainfall rate assimilation sensitivity experiments.

Fig. 1: 19.35 GHZ vertical polarization brightness temperatures (solid line) and the pixels of DMSP F-8 satellite with SSM/I (dots) at about (a) 0000 UTC, (b) 0930 UTC and (c) 2200 UTC 4 January 1989. The fronts are subjective analysis based on the interpolation of the analysis of Neiman and Shapiro (1993)

Fig. 2: Variations of the cost function with the iterations for experiment (a) 3DVC and (b) 4DVC.

Fig. 3: SSM/I-measured (a) precipitable water vapor  $PW$  (mm) and (b) rain rate  $RR$  ( $mm \cdot h^{-1}$ ) at 0000 UTC 4 January 1989; SSM/I-measured (c)  $PW$  (mm) and (d)  $RR$  ( $mm \cdot h^{-1}$ ) at 0930 UTC 4 January 1989; SSM/I-measured (e)  $PW$  (mm) and (f)  $RR$  ( $mm \cdot h^{-1}$ ) at 2200 UTC 4 January 1989. (the magnitude of  $PW$  and the intensity of  $RR$  are indicated by the grey scales on the bottom of the figure).

Fig. 4: (a) Precipitable water vapor  $PW$  (mm) analyzed from the conventional rawinsonde observations by the pre-process of MM5 system, (b) rain rate  $RR$  ( $mm \cdot h^{-1}$ ) generated from a one time step MM5 integration initialized from the analyzed initial conditions. (the magnitude of  $PW$  and the intensity of  $RR$  are indicated by the grey scales on the bottom of the figure).

Fig. 5: 3DVC (a) Precipitable water vapor  $PW$  (mm) and (b) rain rate  $RR$  ( $mm \cdot h^{-1}$ ) at initial time (0000 UTC 4 January 1989); 4DVC (c)  $PW$  (mm) and (d)  $RR$  ( $mm \cdot h^{-1}$ ) at 0000 UTC 4 January 1989, and (e)  $PW$  (mm), (f)  $RR$  ( $mm \cdot h^{-1}$ ) at 0930 UTC 4 January 1989. (the magnitude of  $PW$  and the intensity of  $RR$  are indicated by the grey scales on the bottom of the figure).

Fig. 6: (a) MM5 system analyzed initial conditions of sea level pressure field (solid line, 2-hPa interval) and equivalent potential temperature field at  $\sigma = 0.93$  (dashed line, 4K interval), and the optimal initial conditions of sea level pressure field (solid line, 2-hPa interval) and equivalent potential temperature field at  $\sigma = 0.93$  (dashed line, 4K interval) for assimilation experiment (b) 3DVC and (c) 4DVC. (Line AB in (b) and Line CD in (c) are for the cross-sections in the following figures 7 and 8 respectively).

Fig. 7: The cross-section of the difference fields between the optimal initial conditions of the assimilation experiment 3DVC and control run CTRC along line AB in Fig. 6b (a)  $\Delta T$  cross-section field (K) and (b)  $\Delta q$  cross-section fields ( $g \cdot kg^{-1}$ ).



Fig. 8: The cross-section of the difference fields between the optimal initial conditions of the assimilation experiment 4DVC and control run CTRC along CD in Fig. 6c (a)  $\Delta T$  cross-section field ( $K$ ) and (b)  $\Delta q$  cross-section fields ( $g \cdot kg^{-1}$ ).

Fig. 9: The sea level pressure field (solid line, 2-hPa interval) and equivalent potential temperature field (dashed line, 4K interval) at 0000 UTC 5 January 1989 from the forecast of control experiments (a) CTRC and (b) CTRF.

Fig. 10: Experiment CTRC predicted rain rate  $RR$  ( $mm \cdot h^{-1}$ ) at (a) 0930 UTC and (b) 2200 UTC 4 January 1989 (the intensity of the rain rate is indicated by the grey scales on the bottom of the figure).

Fig. 11: Experiment CTRF predicted rain rate  $RR$  ( $mm \cdot h^{-1}$ ) at (a) 0930 UTC and (b) 2200 UTC 4 January 1989 (the intensity of the rain rate is indicated by the grey scales on the bottom of the figure).

Fig. 12: Predicted Sea level pressure field (solid line, 2-hPa interval) and equivalent potential temperature field (dashed line, 4K interval) at 0000 UTC 5 January 1989 by experiment (a) 3DVC and (b) 4DVC.

Fig. 13: Experiment 3DVC predicted rate  $RR$  ( $mm \cdot h^{-1}$ ) at (a) 0930 UTC and (b) 2200 UTC 4 January 1989 (the intensity of the rain rate is indicated by the grey scales on the bottom of the figure).

Fig. 14: Experiment 4DVC predicted rate  $RR$  ( $mm \cdot h^{-1}$ ) at 2200 UTC 4 January 1989 (the intensity of the rain rate is indicated by the grey scales on the bottom of the figure).

Fig. 15: Moisture divergence at 850 hPa at (a-b) 1200 UTC 4 January and (c-d) 0000 UTC 5 January for 3DVC (left column) and 4DVC (right column). Contour interval is  $2 \times 10^{-7} s^{-1}$ .

Fig. 16: Same as Fig. 15 except for the vertical velocity at 500 hPa. Contour interval is  $5 \text{ cm s}^{-1}$ .

Fig. 17: The 6-hour cyclone track of the ERICA IOP-4 case, predicted by the 50-km experiments initialized at 0000 UTC 4 and terminated at 0000 UTC 5 January 1989. (The solid circle is for observation, star for 50-km control run, open circle for 3DVC and solid square for 4DVC.)

Fig. 18: Simulated 850-hPa wind vector and temperature fields for (a) CTRC and (b) 4DVC at 0000 UTC 5 January 1989, and the differences of latent heating ( $^{\circ}\text{C h}^{-1}$ ) between 4DVC and CTRC at (c) 700 hPa and (d) 500 hPa at 0000 UTC 5 January 1989.

Fig. 19: The 6-hour cyclone track of the ERICA IOP-4 case, predicted by the 25-km experiments initialized at 0000 UTC 4 and terminated at 0000 UTC 5 January 1989. (The solid circle is for observation, star for 25-km control run, open circle for 3DVF and solid square for 4DVF.)

Fig. 20: The 6-hour cyclone intensity variations from 0000 UTC 4 to 0000 UTC 5 January 1989. (the thick solid line is for observation, dotted line for CTRC, short dashed line for CTRF, long dashed line for 3DVC, dot-dashed line for 3DVF, thin solid line with circle is for 4DVC and with dot for the assimilation experiment 4DVF).

Fig. 21: Total precipitation ( $\text{mm}$ ) in the first three hours' simulations for experiment (a) CTRC, (b) 3DVC and (c) 4DVC.

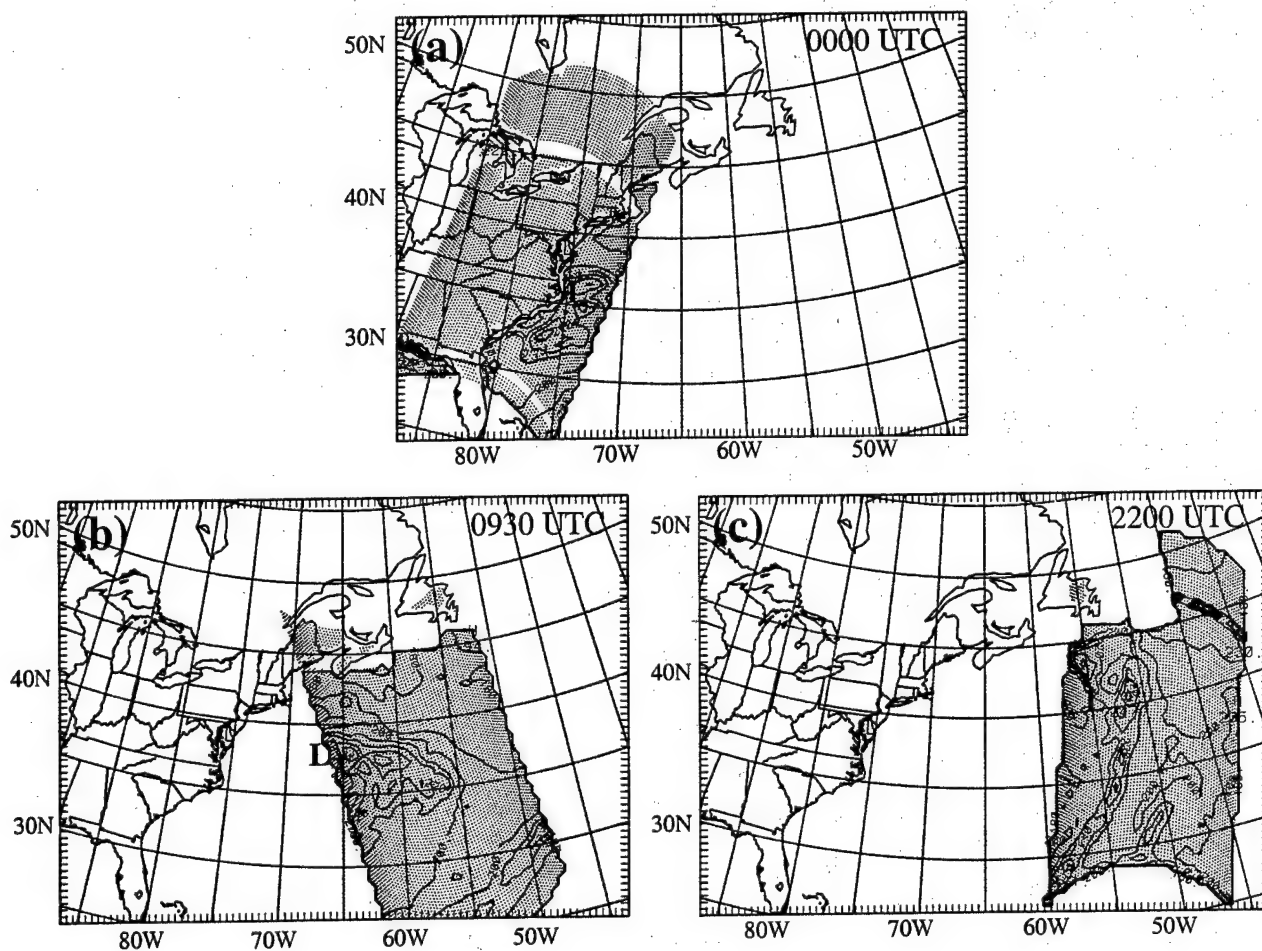
Fig. 22: RMS difference between the sensitivity experiments and the control experiment CTRC within a 1000 km square area centered at the cyclone center (Solid line is for experiment A, dotted line for experiment B, short dashed line for experiment C, long dashed line for experiment D and the dot-dashed line for experiment E)

Table 1: SSM/I precipitable water and rainfall rate assimilation experiments

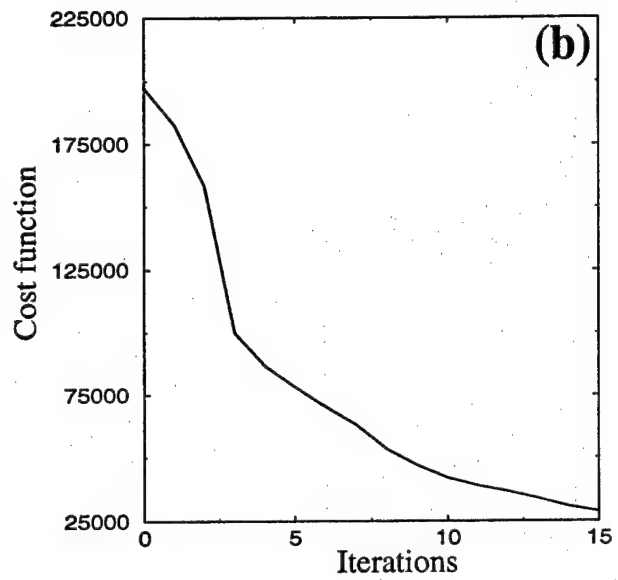
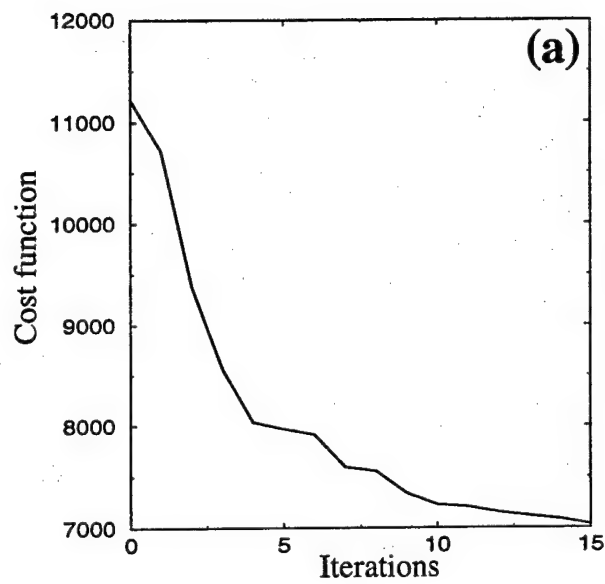
Experiment	Horizontal resolution (km)	Minimization			IC (Simulation)	24-h Intensity (hPa)	24-h Position Error (Km)
		Guess IC	Period (UTC)	Observation			
CTRC	50				MM5 Analysis	940	263
CTRF	25				MM5 Analysis	935	204
3DVC	50	MM5 Analysis	0000-0000	SSM/I PW,RR	Optimal IC	941	159
4DVC	50	MM5 Analysis	0000-0930	SSM/I PW,RR	Optimal IC	944	42
3DVF	25				Intp. from 3DVC	935	90
4DVF	25				Intp. from 4DVC	936	26
OBS						936	

Table 2: SSM/I rainfall rate assimilation experiments

Experiment	Assimilation Method	Cumulus Scheme	SSM/I RR Time (UTC)	Forcing Period (UTC)	RR Errors	24-h Intensity (hPa)	24-h Position Error (Km)
A	4DVAR	Grell	0000 and 0930			938	185
B	4DVAR	Grell	0000 and 0930		-10%	937	229
C	4DVAR	Grell	0000 and 0930		-20%	936	229
D	4DVAR	Grell	0000 and 0930		-40%	936	229
E	4DVAR	Grell	0000 and 0930		300Km	938	263
F	No	Kuo				943	263
G	4DVAR	Kuo	0000 and 0930			943	213
H	Heating Replace	Kuo	0000 and 0930	0000-0300 0630-1230		943	263
OBS						936	



**Fig. 1**



**Fig. 2**

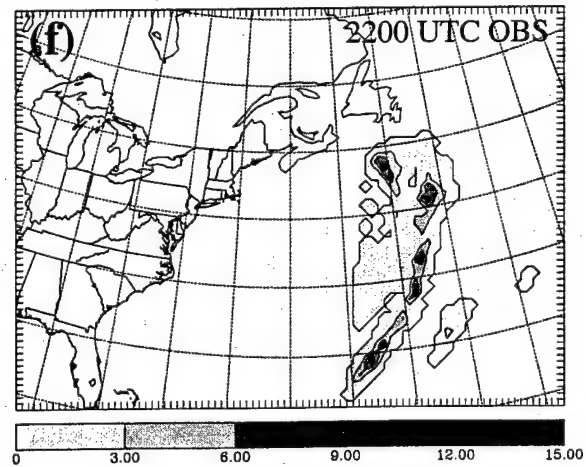
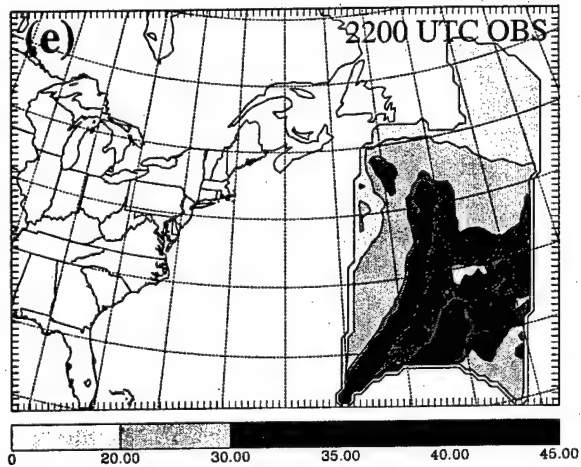
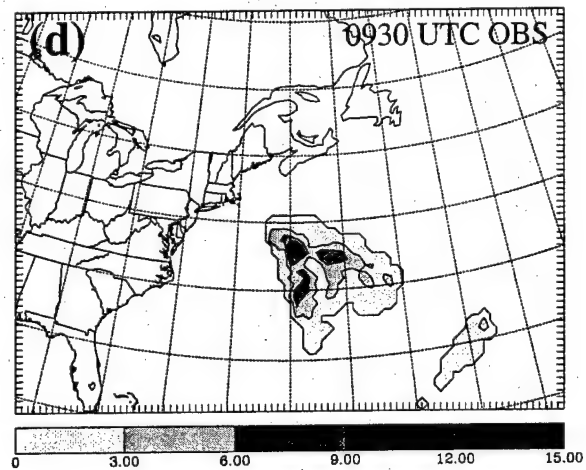
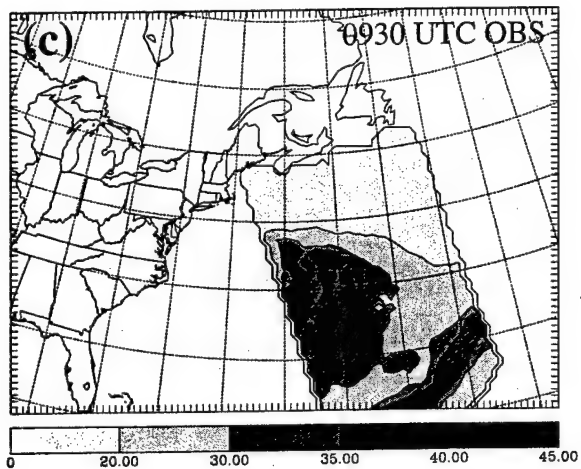
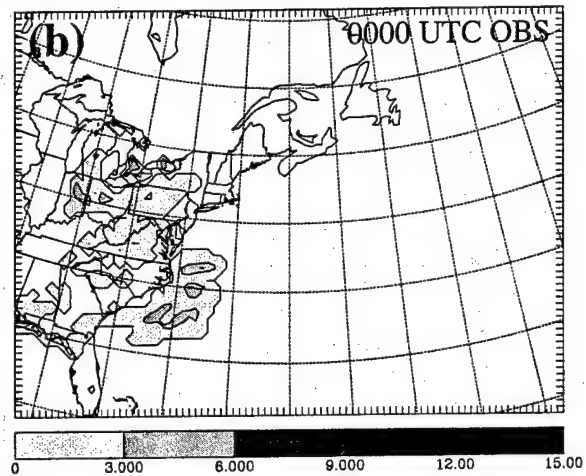
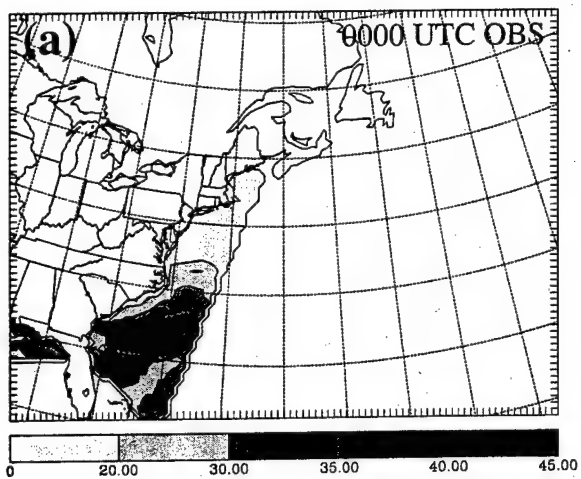
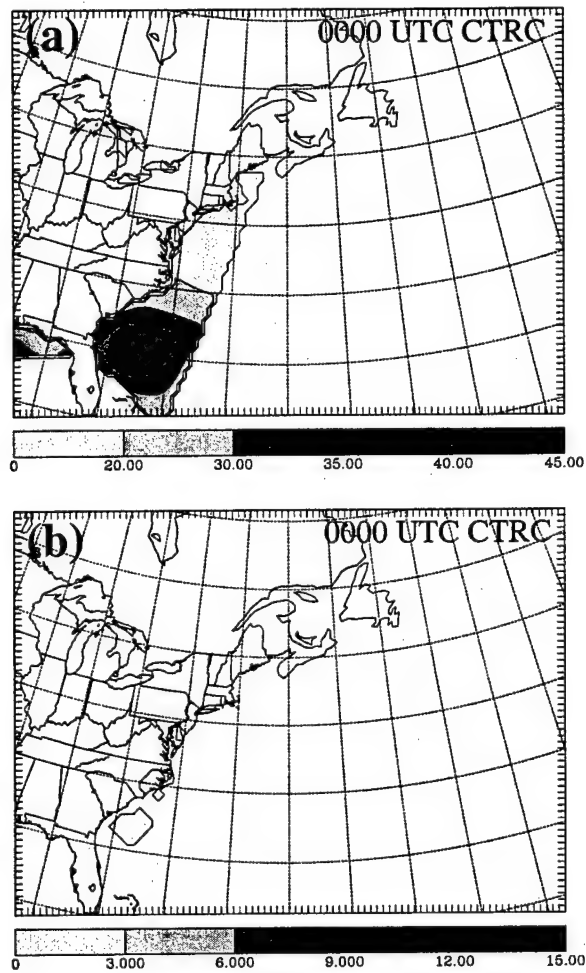


Fig. 3



**Fig. 4**



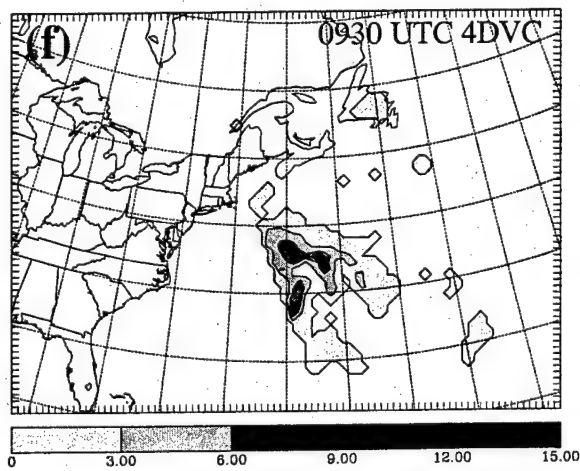
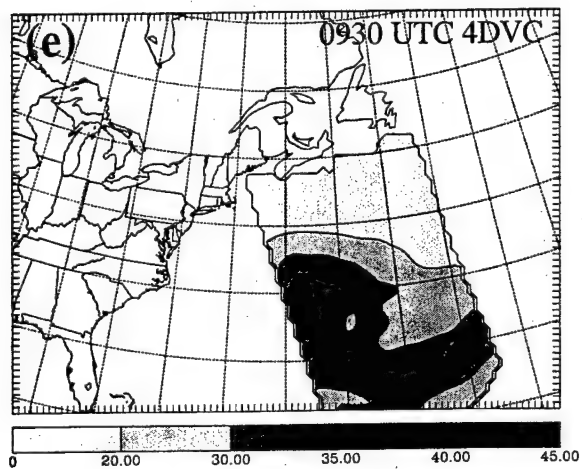
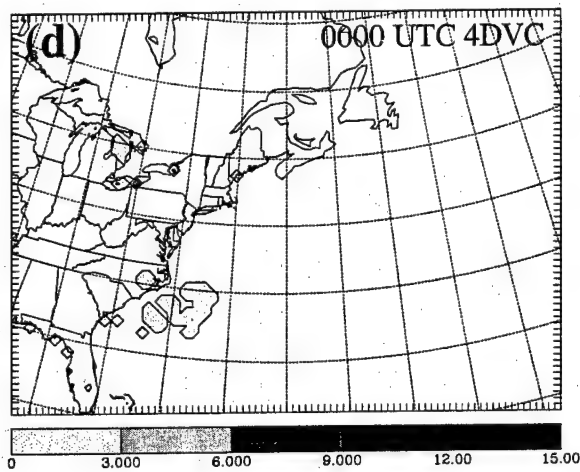
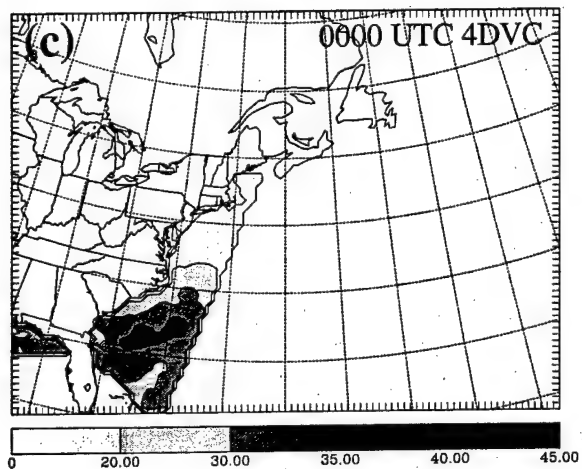
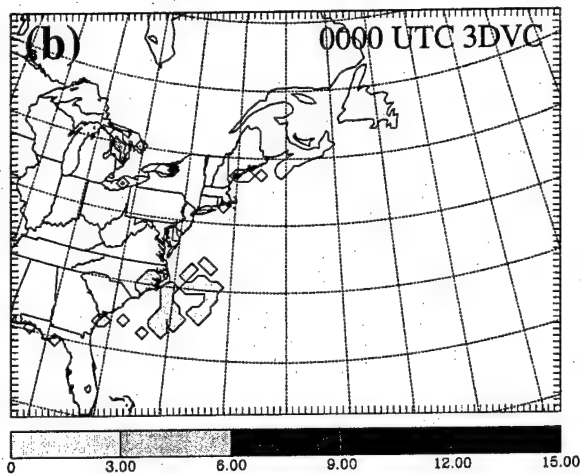
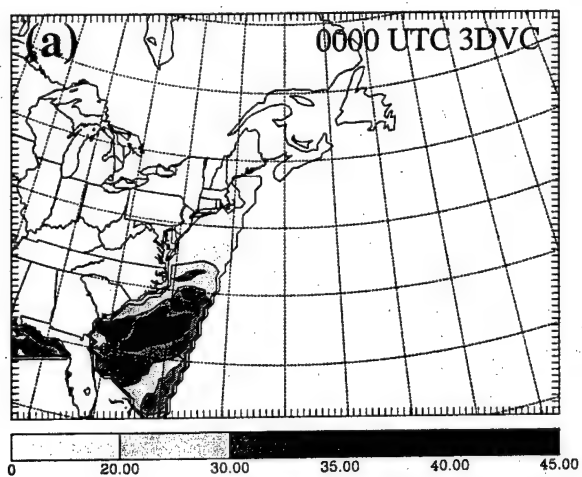
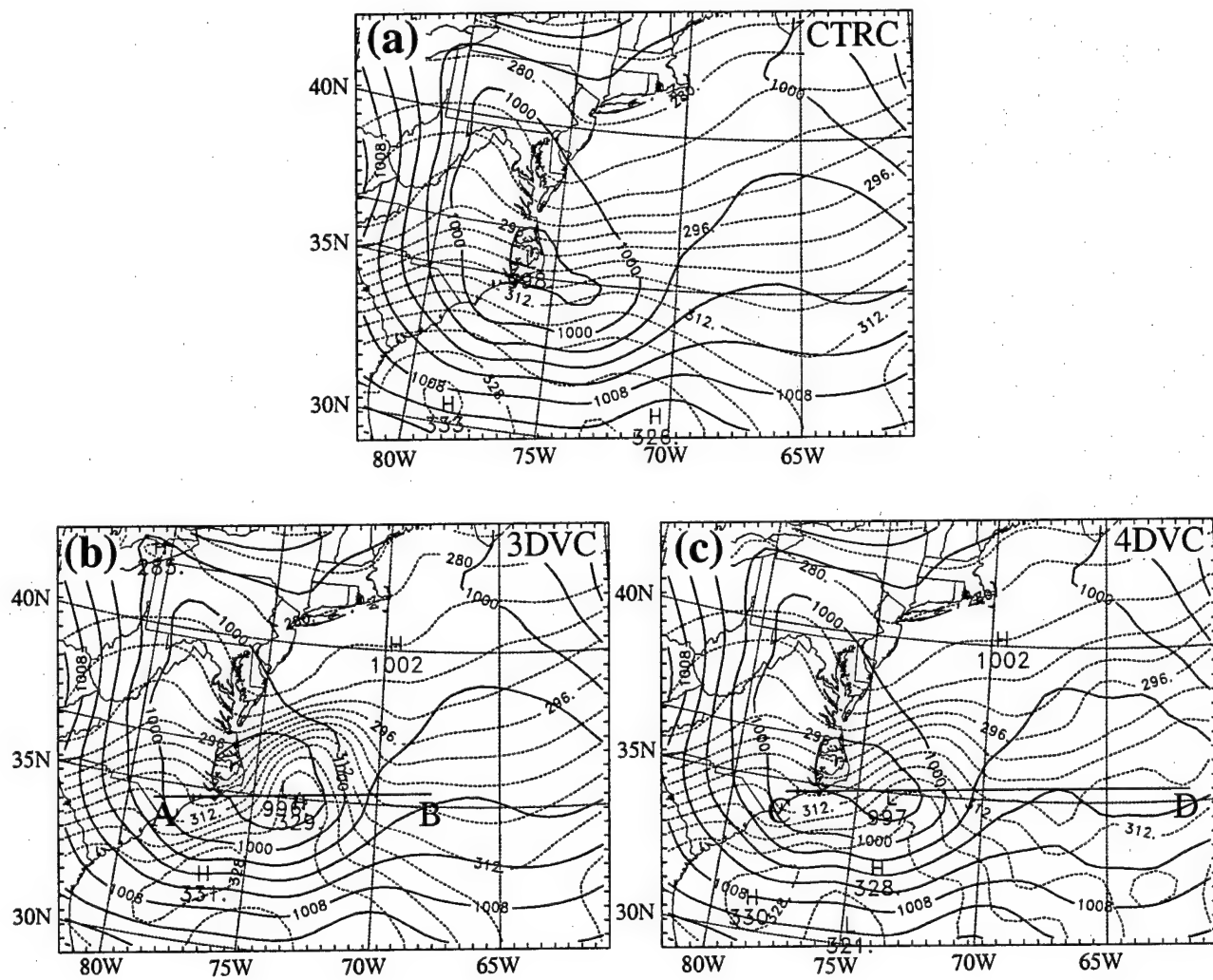
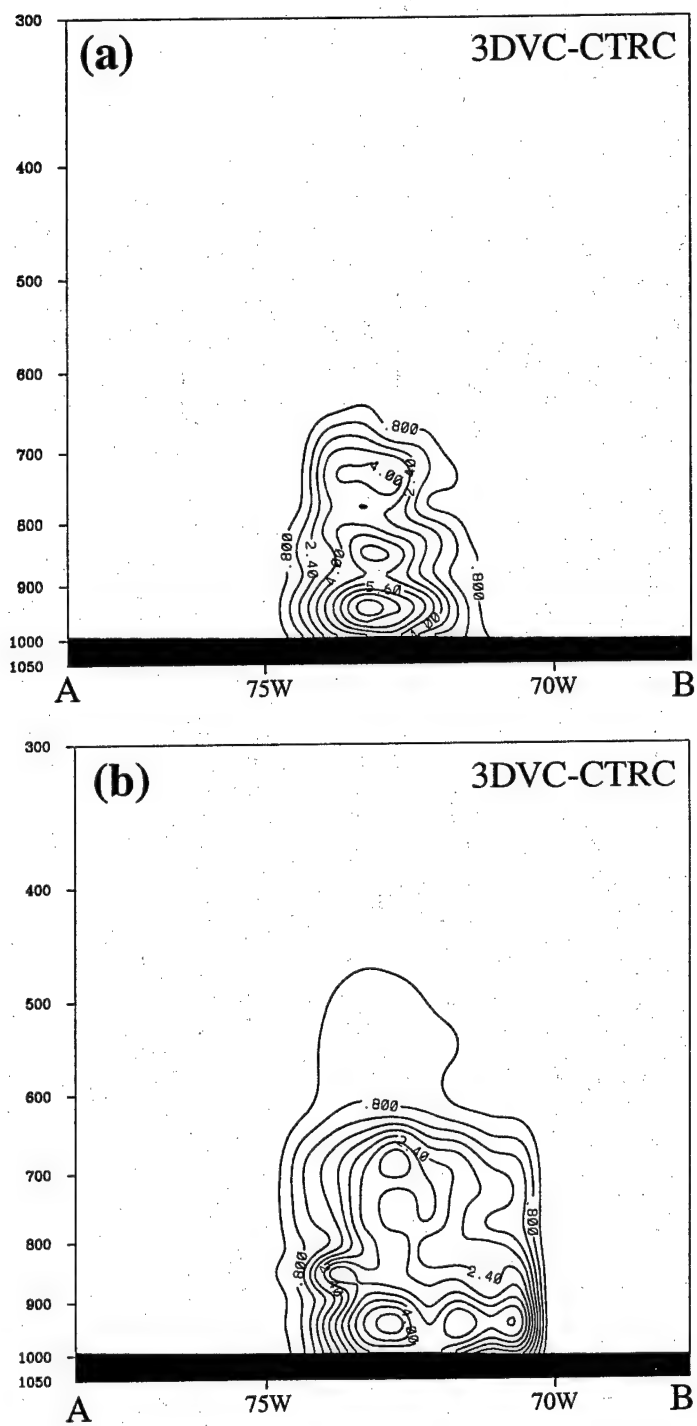


Fig. 5



**Fig. 6**



**Fig. 7**

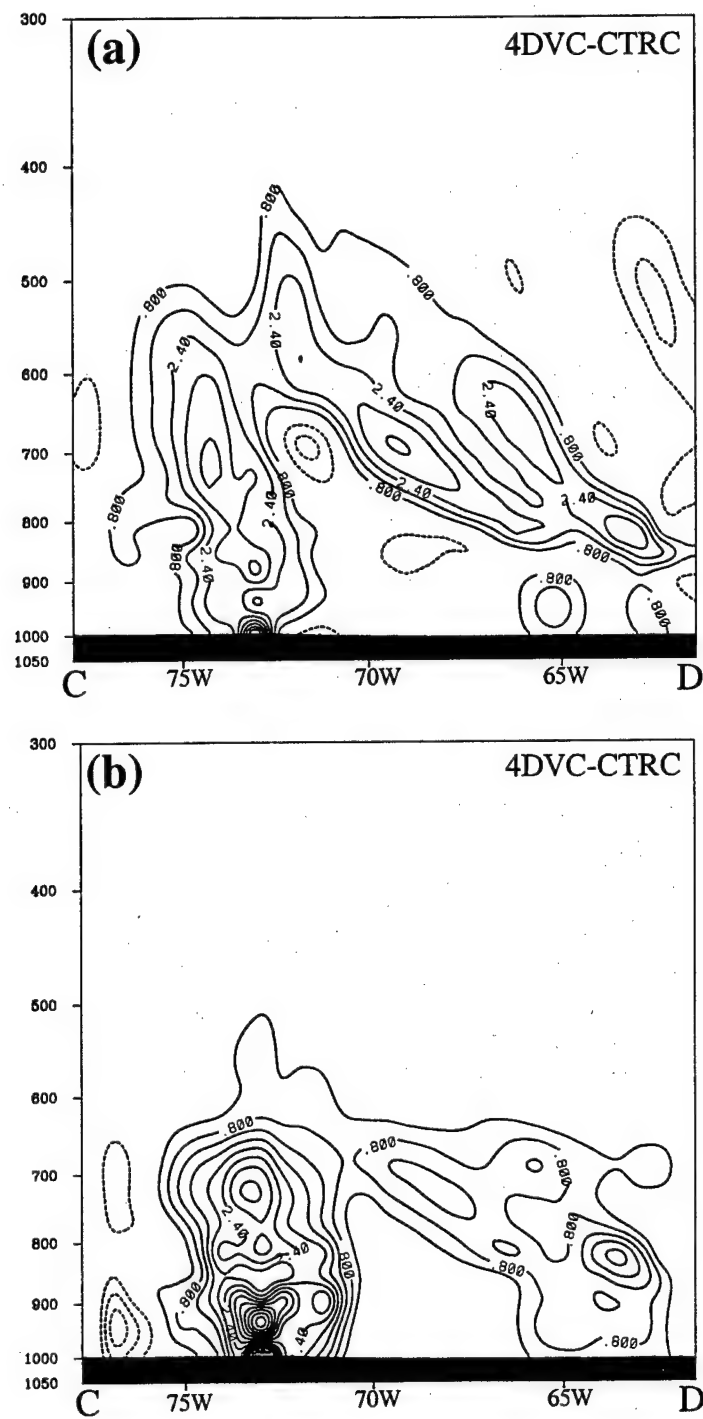


**Fig. 8**



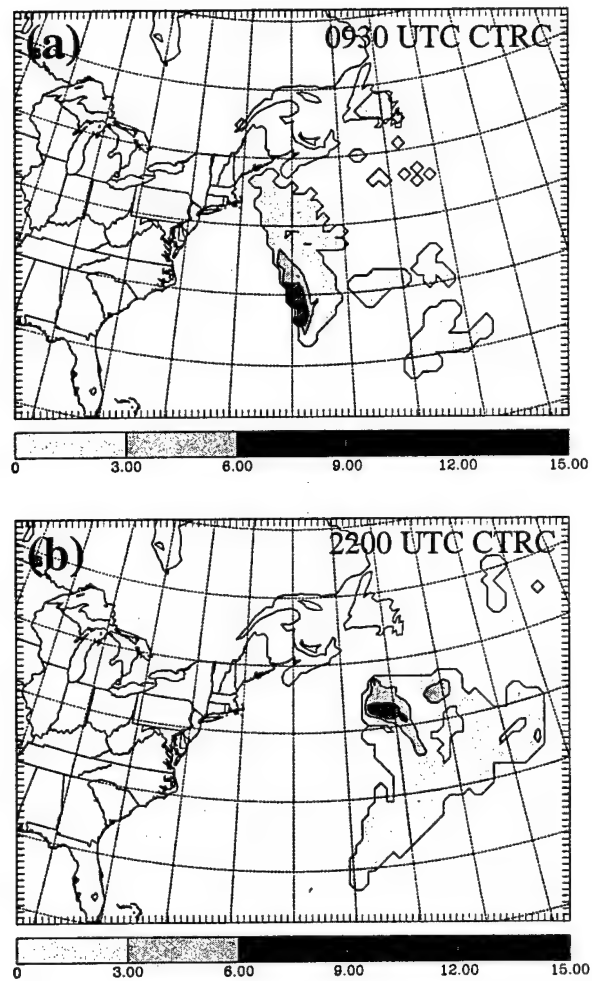


**Fig. 10**

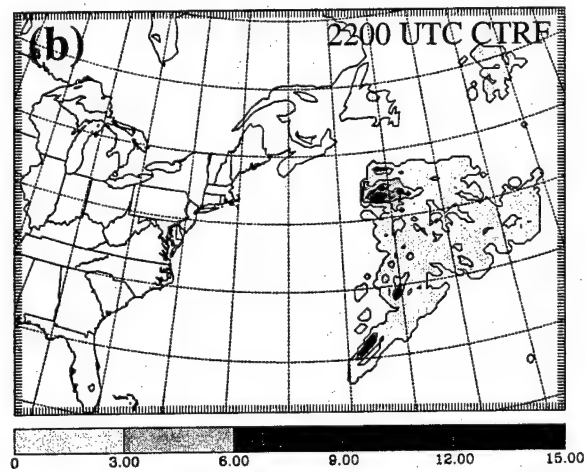
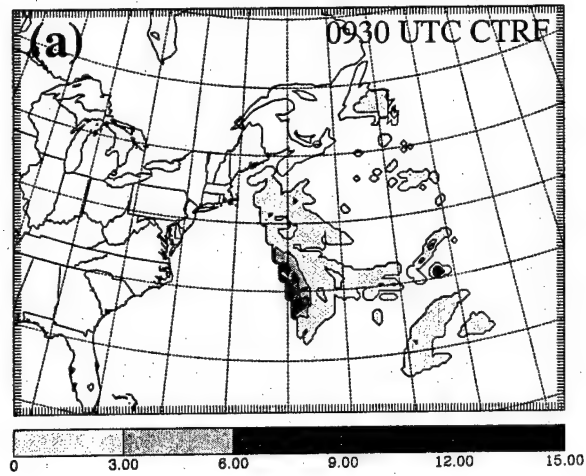
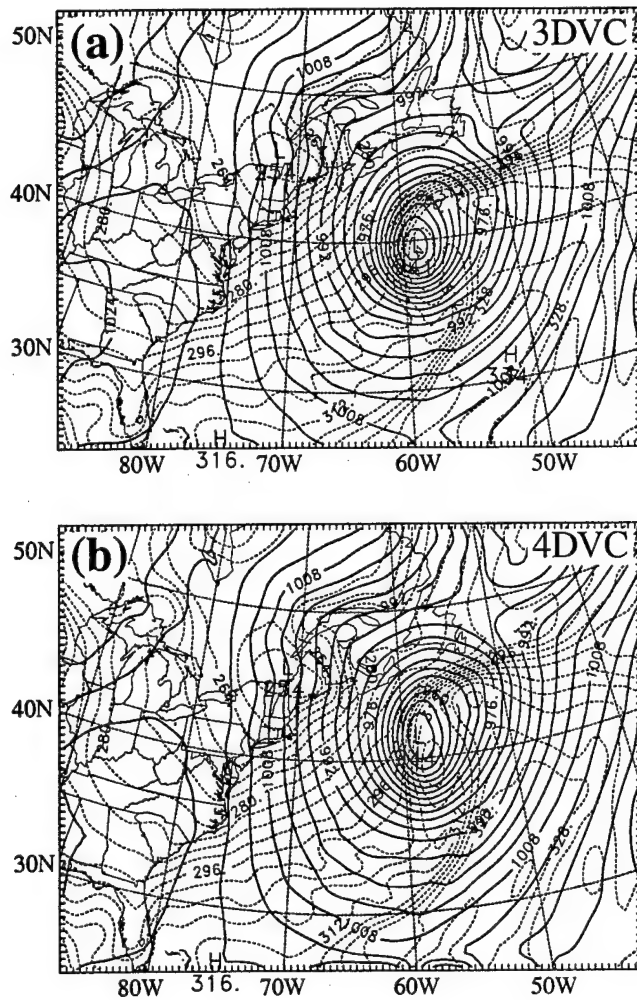
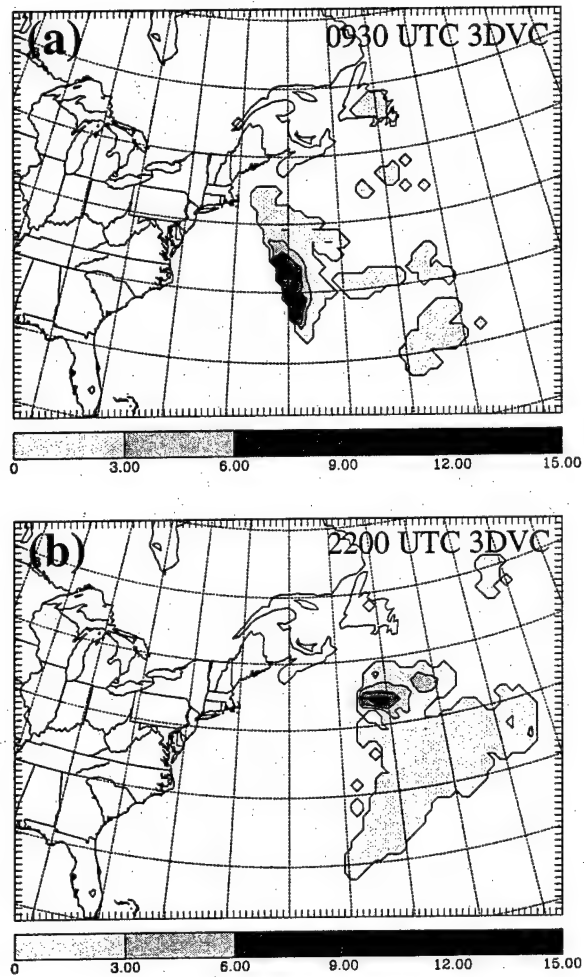


Fig. 11







**Fig. 13**

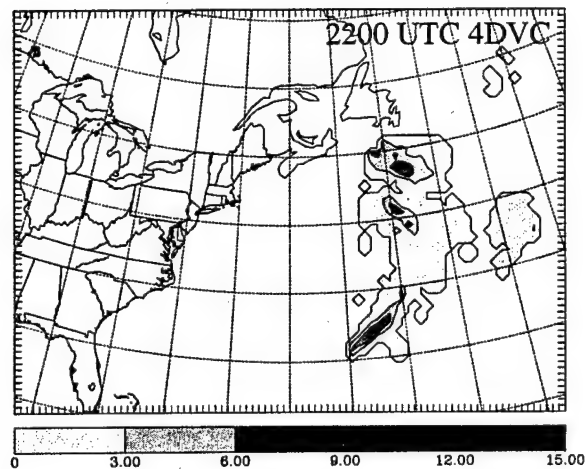


**Fig. 14**

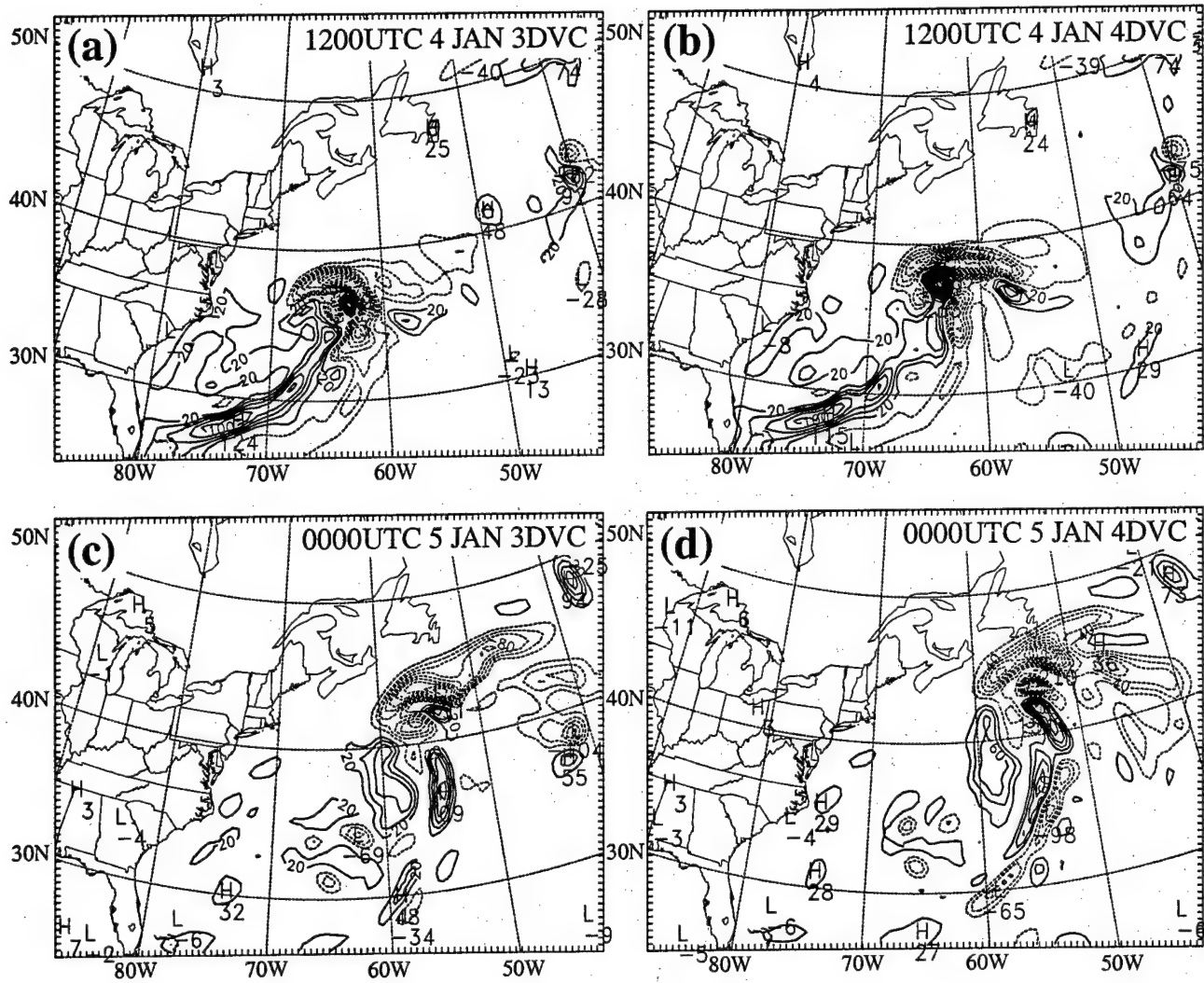


Fig.15

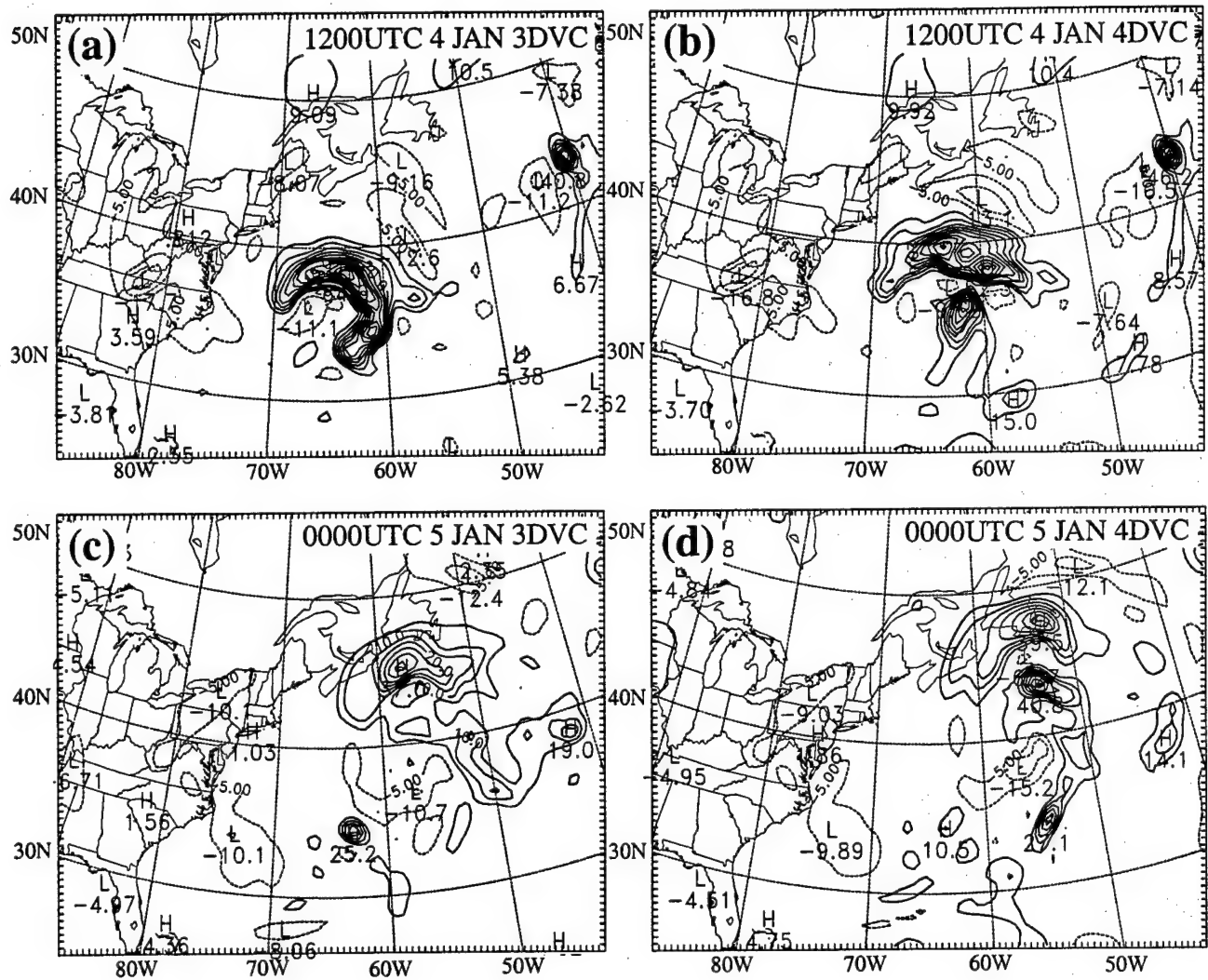


Fig.16

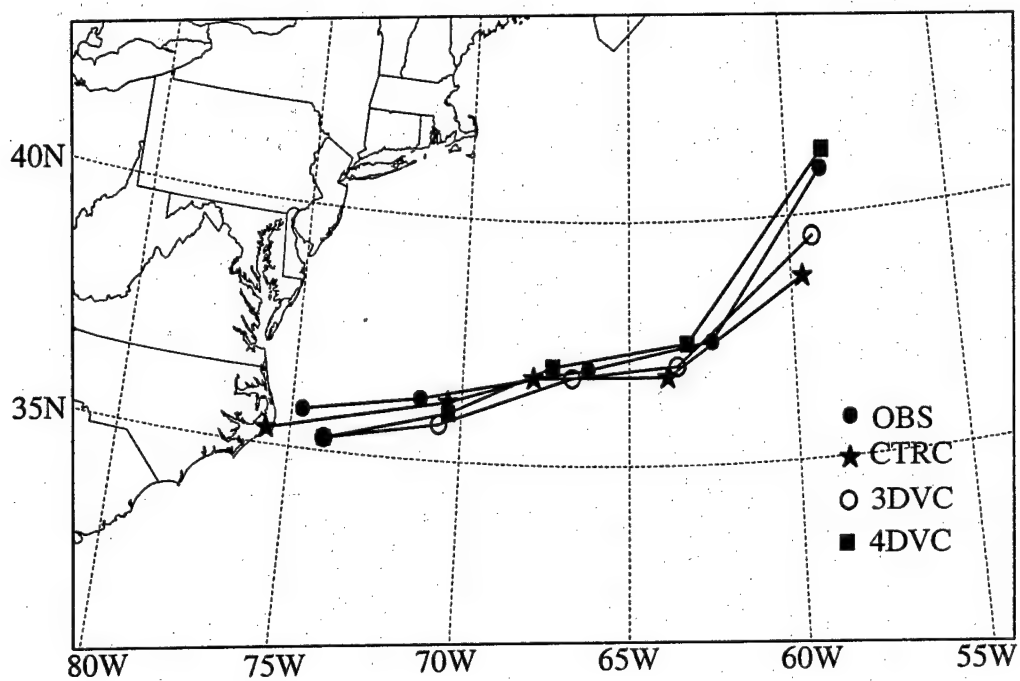


Fig. 17

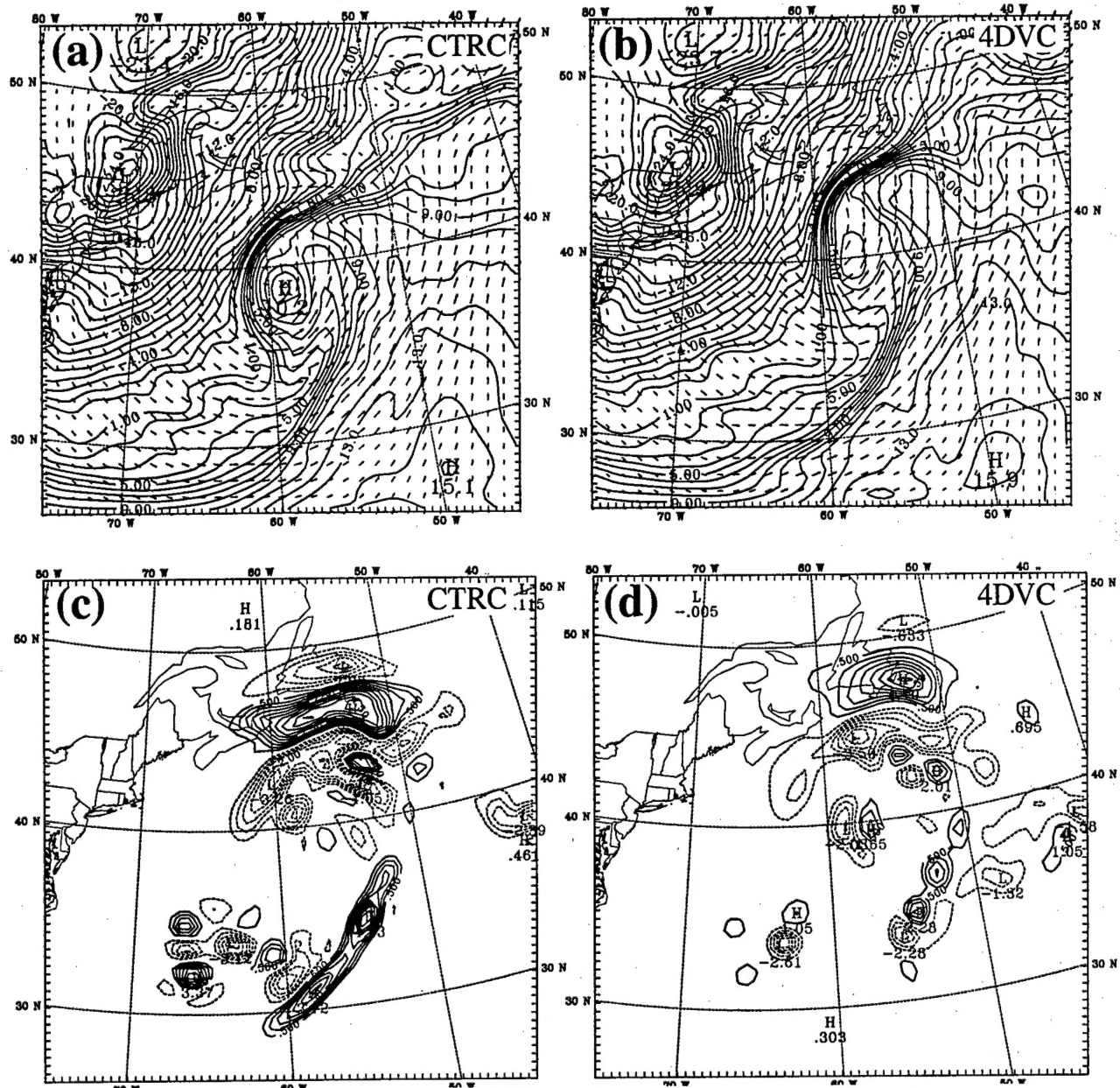


Fig. 18

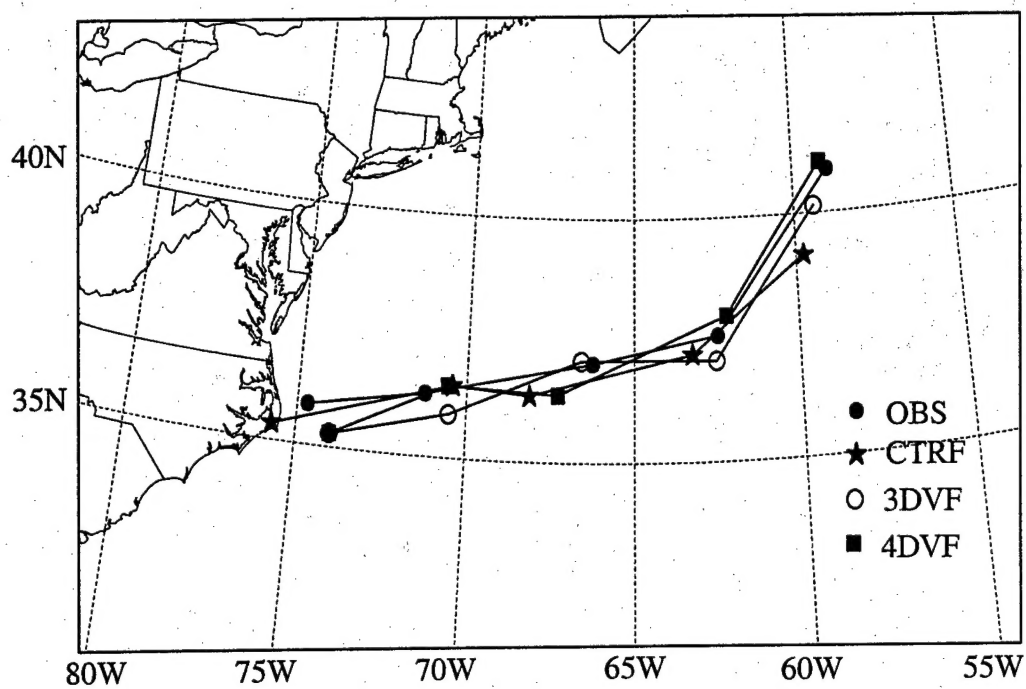


Fig. 19

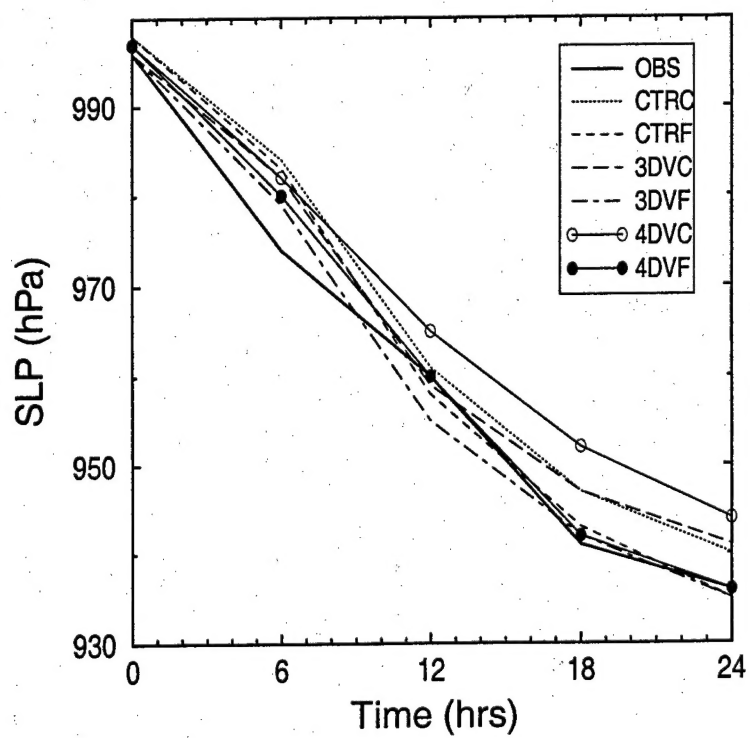


Fig. 20

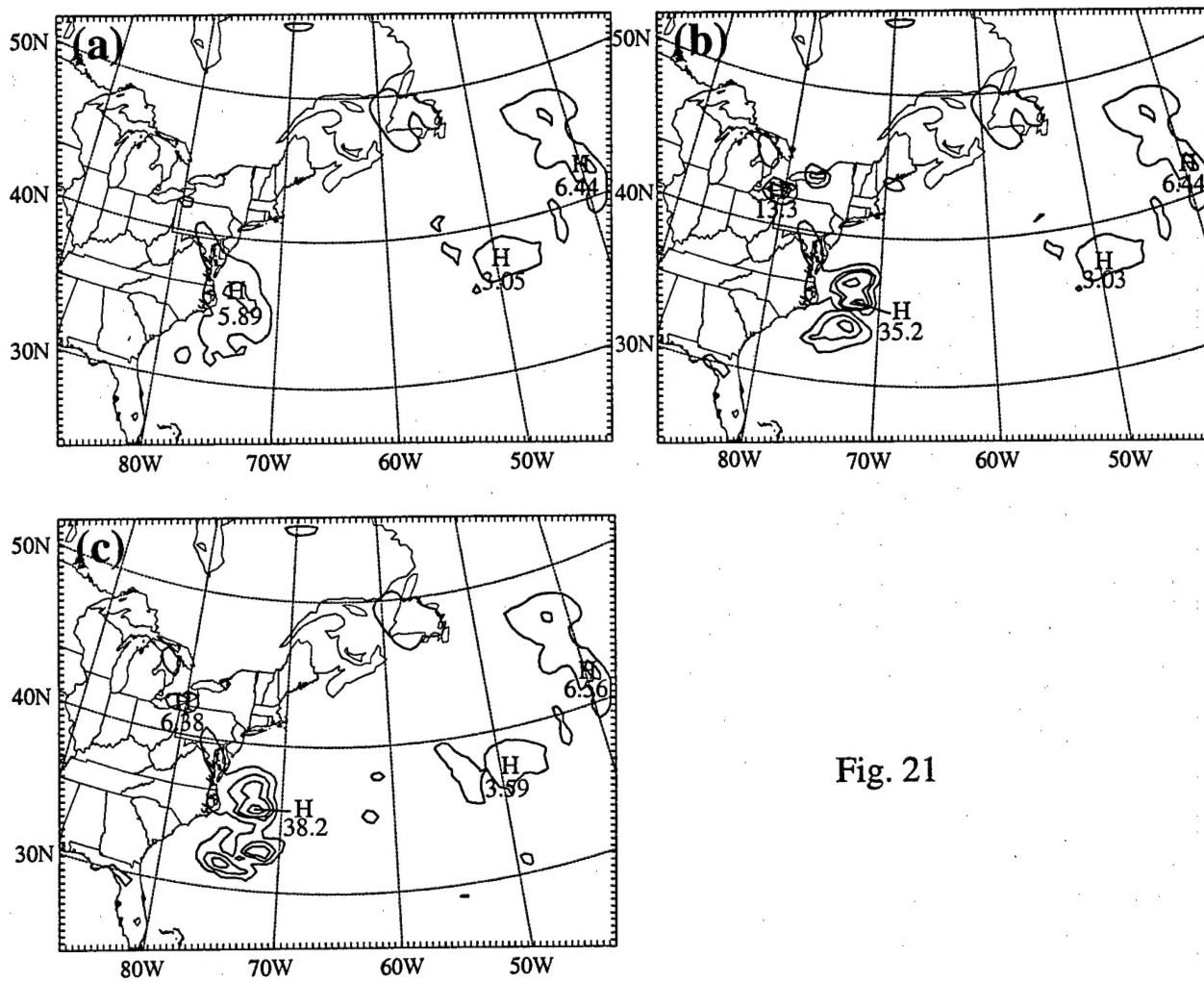


Fig. 21



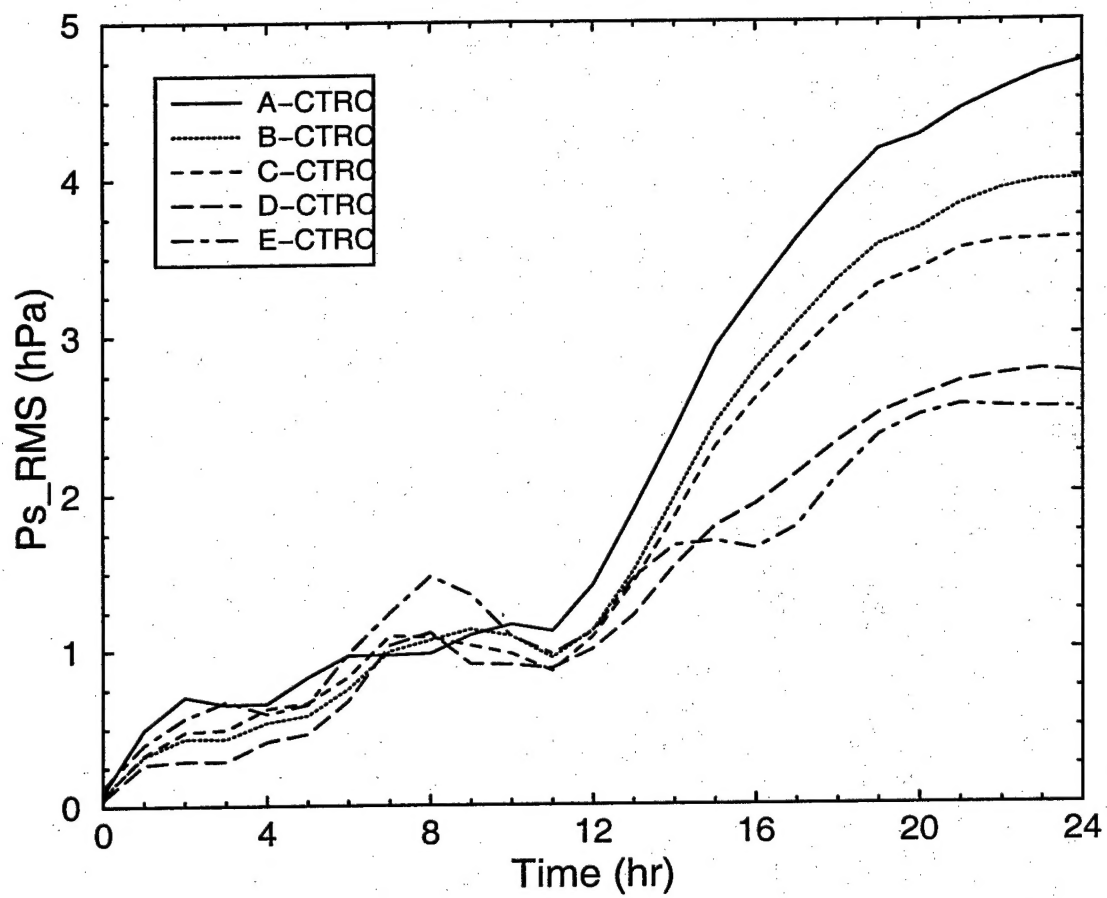


Fig. 22